Chapter 3   Convective Instability in the Martian Middle Atmosphere

3.1 Introduction

The Mars Climate Sounder (MCS) on Mars Reconnaissance Orbiter (MRO) [*McCleese et al.*, 2007] has observed Mars's atmosphere and surface for 1.5 martian years. The radiance data collected by MCS can be used to retrieve temperature profiles of moderate resolution (~5 km) from the surface to deep in the middle atmosphere (~85 km). Thus, MCS bridges the gap between temperature sounding nearer the surface provided by past nadir infrared spectroscopy and radio occultation, and measurements in the upper atmosphere from aerobraking experiments, stellar occultation, and other techniques. MCS's ability to map the thermal structure of the middle atmosphere globally also may allow it to detect and map dry convective instabilities within the middle atmosphere: a phenomenon of interest for martian middle atmospheric dynamics and comparative planetology with the Earth.

Since the 1960s [e.g., *Knudsen and Sharp*, 1965; *Hodges*, 1967; *Lindzen*, 1981; *Whiteway and Carswell*, 1994; *Sica and Thorsley*, 1996; *Williams et al.*, 2002], dry convective instabilities have been observed throughout the Earth's stratosphere and mesosphere in association with wave-like perturbations. Recent studies in the terrestrial extratropics have observed convective instabilities in thermal profiles and/or convective roll structures near the mesopause [*Collins and Smith*, 2004; *Liu et al.*, 2004; *Williams et al.*, 2006], which they interpret to result from superposition of internal gravity waves with the thermal tides. The large amplitudes of the thermal tides on Mars [*Zurek*, 1976; *Lee et al.*, 2009] and suspected tidal filtering of gravity waves observed in Mars's upper

atmosphere [*Wang et al.*, 2006] suggest that such tidal-gravity wave interactions may occur on Mars.

The wave dissipation due to such interactions (or the unstable breakdown of tides or gravity waves alone) could be a potent source of turbulent drag and force vigorous meridional circulations within Mars's middle atmosphere, potentially driving the strong temperature inversion observed in the middle atmosphere near the winter pole [e.g., *Deming et al.*, 1986; *McCleese et al.*, 2008]. This idea was first explored in depth by *Jaquin* [1989] and *Barnes* [1990] and expanded upon primarily in modeling work [*Theodoré et al.*, 1993; *Joshi et al.*, 1995; *Collins et al.*, 1997; *Forget et al.*, 1999; *Forbes and Miyahara*, 2006; *Hartogh et al.*, 2007], but observational constraints on tidal and gravity wave drag within Mars's atmosphere remain limited.

Present observational constraints on gravity wave activity come from analyses of Mars Global Surveyor (MGS) Radio Science (RS) lower atmospheric temperature profiles [*Creasey et al.*, 2006], which are restricted to the equator and the summer hemisphere, where weak zonal winds may inhibit the vertical propagation of waves into the middle atmosphere. The accelerometers of aerobraking spacecraft are sensitive to density fluctuations due to both tides and gravity waves in the upper atmosphere. Using data from MGS and Mars Odyssey (ODY) accelerometry, *Fritts et al.* [2006] estimates gravity wave momentum fluxes per unit mass in the upper atmosphere at 95-130 km to be at least an order of magnitude greater than those on the Earth and infer that gravity waves experience dissipation to considerable depth in the atmosphere.

Modeling studies such as *Barnes* [1990] suggest that the wave drag critical for middle atmospheric polar warmings is below the level observed by *Fritts et al.* [2006],

above the level observed by *Creasey et al.* [2006], and within the winter extratropics,

where the strong westerly zonal jets should enhance the transmission of gravity waves

vertically. Thus, the broad vertical range of MCS retrievals is well situated to look for dry

convective instabilities that could result from tidal or gravity wave dissipation in the

martian middle atmosphere and provide potentially more dynamically relevant

constraints on the forcing of the circulation due to these phenomena.

In this study, we will use MCS temperature retrievals to detect and map regions of

convective instability. In Chapter 3.2, we describe the retrieval dataset and its analysis. In

Chapter 3.3, we investigate spatiotemporal variability in convective instability in the

middle atmosphere. In Chapter 3.4, we consider the driving mechanisms for the observed

instabilities and implications of the observed instabilities for atmospheric dynamics. In

Chapter 3.5, we summarize our results.

3.2 Data and Analysis

3.2.1. Dataset

MCS is a limb and on-planet scanning filter radiometer [*McCleese et al.*, 2007]. It

measures thermal emission in the mid- and far infrared wavelength range. Using the

measured radiances, vertical profiles of temperature, pressure, dust and water ice

currently are retrieved over an altitude range from ~10 to 85 km at a vertical resolution of

~5 km as described in detail by *Kleinböhl et al.* [2009]. The retrieval product contains an

error estimate for each retrieved profile. The temperature error estimate is calculated by

finding the radiance difference due to a small temperature perturbation at each altitude

level and scaling it by the root sum of the squares (RSS) of the instrument noise and

the residual radiance that cannot be fit by the retrieval algorithm [*Kleinböhl et al.*, 2009].

Due to instrument issues [*Kleinböhl et al*., 2009], the MCS observations during

L_s=180°—255° of Mars Year 28 (MY 28, as defined by *Clancy et al.* [2000]) are of

lower quality (limb staring). The altitude coverage is limited to below ~50 km in the

southern hemisphere and above ~15 km over the north pole. In addition, the calibration is

not as good during this time and the uncertainties are larger in regions with low

radiances, especially near the top of the MCS coverage. The retrieved temperature

profiles during this period do agree well with profiles immediately afterwards [*Kleinböhl

et al.,* 2009]. Due to MRO issues, MCS observations are not available after L_s=328° in

MY 29.

To assemble a full martian year for study, we primarily use L_s=0° to 328° of MY

29 and L_s=328° to 360° of MY 28. The observations during L_s=110°—168° of MY 28

are used to supplement the observations of MY 29 for northern spring and summer.

These seasons are thought to have limited interannual variability [*Richardson*, 1998;

Wilson and Richardson, 2000; *Cantor et al.*, 2002; *Liu et al.*, 2003]. After accounting for

the bias in the altitude coverage, we use the retrieved profiles from limb staring

observations and observations during the remainder of MY 28 (through L_s=328°) for

interannual comparisons in the southern spring and summer seasons.

The current retrieval algorithm [*Kleinböhl et al.*, 2009] does not attempt to

retrieve high haze layers. If given a radiance profile from an atmosphere with a haze

layer, it will introduce an artificial temperature minimum and/or maximum. This usually

produces a very sharp inversion in the temperature profile resulting in an artificially

unstable lapse rate. The temperature of this inversion is significantly warmer than

nearby profiles. While the retrieval processing is designed to avoid retrieval near high

hazes, some still may cause problems.

Inspection of radiance profiles suggests that high hazes are very rare in the

extratropics during the winter. The tropics are far more affected (see Chapter 3.3.1). The

high hazes in this region may be equatorial mesospheric clouds such as those recently

described by *Clancy et al.* [2007], *Montmessin et al.* [2007], and *Inada et al.* [2007].

Note that condensation in the cold phase of vertically propagating gravity waves is one

possible origin of high hazes, so there may be preferential exclusion of retrievals in

regions of intense gravity wave activity.

MCS's vertical resolution of ~5 km should be sufficient to resolve zones of

convective instability in the middle atmosphere due to thermal tides and gravity waves.

High resolution observations of gravity wave driven instabilities in the Earth's

atmosphere suggest the instabilities have a fractal character: longer gravity waves/tides

saturate to produce 5—15 km zones of neutral or near-neutral stability that are genuinely

unstable at higher resolution due to perturbations by smaller-scale waves [*Williams et al.*,

2006]. On Mars, a hypothetical longer wave could be one phase of the diurnal thermal

tide with a vertical wavelength of ~30 km, such that a gravity wave with a wavelength as

short as 10 km might produce a resolved instability. We assess horizontal sensitivity by

considering an instability arising from superposition of a tide with a gravity wave

propagating within a two-dimensional plane.

For medium frequency waves, the vertical wavelength of a gravity wave is

~$2\pi[|(u-c)|/N]$, where u is the mean wind, c is the phase speed, and N is the Brunt-Väisälä

frequency [*Fritts and Alexander*, 2003]. In Mars's middle atmosphere, N is $\sim 10^{-2}$ s, so vertical wavelengths of 10-30 km will correspond to stationary waves ($c=0$) in a mean wind of 15—45 ms^{-1}. So this investigation should be especially sensitive to convective instabilities due to waves under these mean wind conditions, depending on phase speed.

Each MCS retrieval is averaging over an atmospheric slice ~10 km wide by ~300 km long (narrowing to ~100 km near the surface). It can be considered a locally vertical profile when analyzing regions of convective instability in the middle atmosphere, despite the overall lengthwise variability in weighting function peaks between the surface and 80 km [cf. *Kleinböhl et al.*, 2009, Figure 12]. The orientation of the slice depends on the time of day (or latitude) of the observation. Over most of the planet, the long direction is primarily north-south (slightly west of north on the dayside and slightly west of south on the night side). Over the poles, the long direction is oriented westward. MRO's orbital velocity of 3 km/s is sufficiently fast that the MCS observations capture the instantaneous appearance of the atmosphere, especially gravity waves. In the current observation mode, with ~30 s between retrieved profiles, individual profiles overlap by 50% with their nearest neighbors.

For gravity waves with relevant vertical wavelengths, the horizontal wavelength in the direction of propagation will be a significant fraction of the long dimension of the slice observed by MCS. Thus, the convective instability due to the breaking of a gravity wave traveling parallel to the MCS view direction (usually meridional) should be easily detected. Those traveling perpendicular to the MCS viewing direction (usually zonal) will be more difficult to see since the instability will be averaged with the adjacent stable atmosphere. Large groups of parallel zonal gravity waves breaking at the same altitudes

would be readily discernable. Thus, except for very high latitudes, MCS observations and retrievals are expected to be more sensitive to the convective instability due to the breaking of meridionally propagating waves than that due to zonally propagating waves. See *Wu and Waters* [1996] for an analogous analysis of sensitivity.

To avoid biasing of zonal averages by heavier sampling at particular longitudes, the retrievals and quantities derived from them (as described in Chapter 3.2.2) are binned in 36 (5° resolution) latitudinal bins, 64 (5.625° resolution) longitudinal bins, and L_s bins at 5° resolution. This spatial resolution is comparable to Mars general circulation model grids in space and about as fine in time as possible to permit the bins to be filled, given the MCS observation pattern and a completely successful retrieval algorithm. Due to the limited local time sampling, the observations are further separated into dayside (9:00—21:00 LST) and nightside (21:00—9:00 LST) bins, centered at MRO's nominal 3:00/15:00 LST orbit [*Zurek and Smrekar*, 2007].

The variability in the longitudinal sampling of the retrieval dataset is depicted in Figure 3.1. Sampling is controlled by a variety of factors, some of which are intrinsic to the data as collected by the instrument, e.g., periods in which data was not collected because the instrument was stowed (no or little longitudinal sampling at all latitudes) and some of which are related to the present limitations in the retrieval algorithm, e.g., the exclusion of retrievals with large residual errors due to the neglect of scattering in the current retrieval procedure (no or limited longitudinal sampling at particular latitudes).
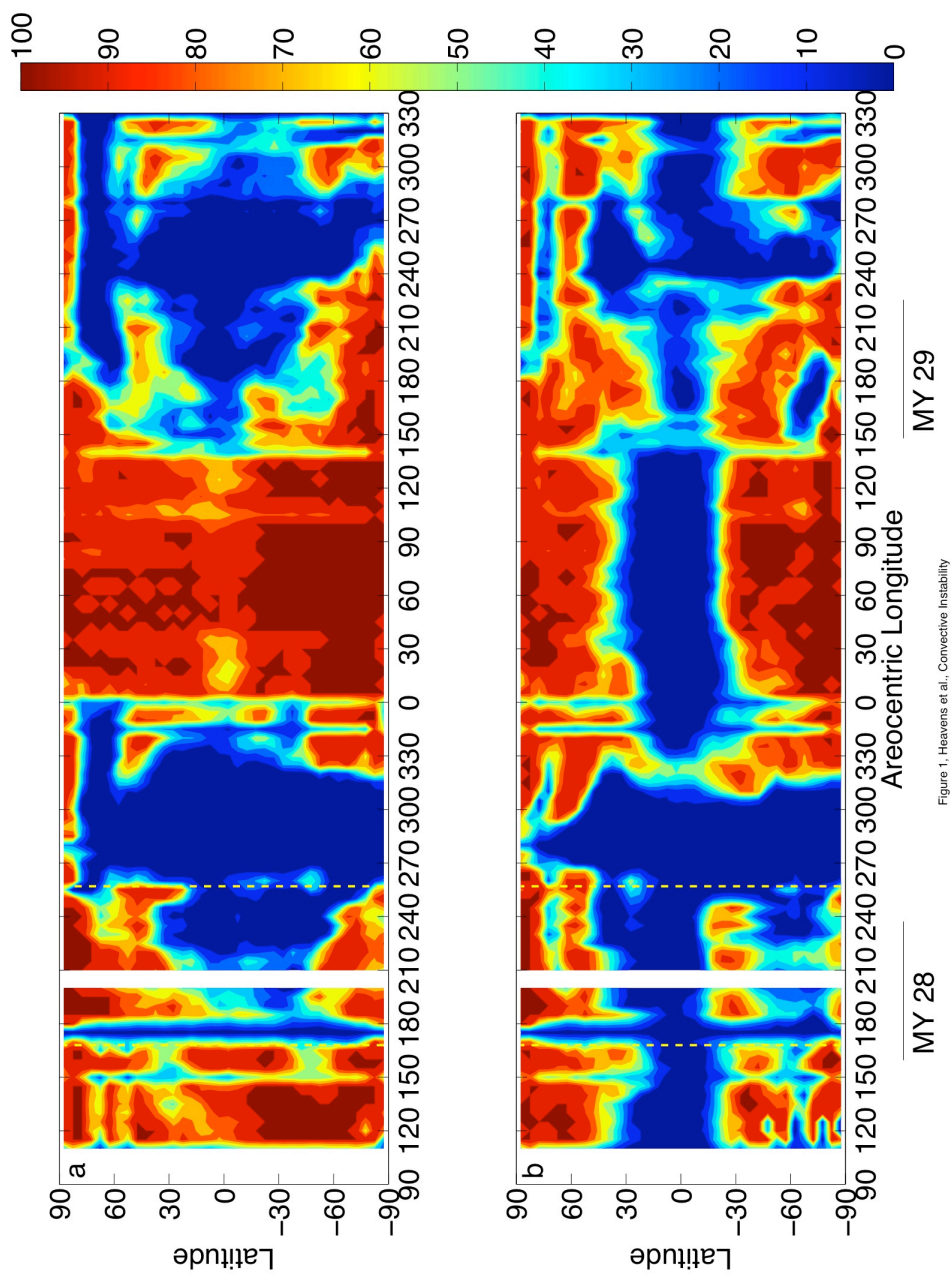
Figure 3.1. Percentage of longitudinal bins with successful MCS retrievals for each L_s/latitudinal bin as described in the text. The dashed yellow lines denote the period of limb staring: (a) nightside; (b) dayside. Contours are every 10%.

3.2.2 Analysis

Convective instability is quantified in two ways: (1) by calculating the difference, $\Gamma(p)$,

between the dry adiabatic lapse rate and the lapse rate at each pressure level in a retrieved

temperature profile using a hydrostatic height coordinate; and (2) by calculating the

maximum Convective Available Potential Energy (CAPE) [*Holton*, 2004] in the middle

atmosphere, $CAPE_{MA}$, at pressures less than 50 Pa in the retrieved temperature profile.

The 50 Pa criterion ensures that convective instabilities in the middle atmosphere are

easily distinguished from the convective boundary layer in the lower atmosphere. *Hinson

et al.* [2008] has shown that the depth of the convective boundary layer is up to 10 km

above high altitude regions such as Tharsis, so a pressure cutoff corresponding to ~25 km

above the datum is reasonable.

In calculating $CAPE_{MA}$, it is assumed that the buoyancy in the temperature profile

arises from the adiabatic cooling of a hypothetical parcel of air at a temperature, T_p,

within the observed superadiabatic environment. Let the base of the superadiabatic region

be at a height, z_b. The parcel cools adiabatically at z_b and begins to rise, since it is more

buoyant than the environment. The parcel continues to rise until some height, z_t, above

the top of the superadiabatic region where the parcel is neutrally buoyant. Thus, in height

coordinates:

$$CAPE_{MA} = \int_{z_b}^{z_t} -g(z) \frac{T_p(z) - T(z)}{T(z)} dz \qquad (3.1)$$

The dry adiabatic lapse rate is $-g/c_p$, where g is the acceleration due to gravity

and c_p is the isobaric heat capacity, but g may vary ~5% within the vertical range of the

profile and c_p may vary by around a factor of 2 over a temperature range of 100—250 K

[*Bücker et al.*, 2003]. We make a first order correction to *g* using altitude information derived from the geometric pointing of the instrument. The isobaric heat capacity is approximated by the zero pressure isobaric heat capacity of CO_2 as modeled by *Bücker et al.* [2003] but with simplified piecewise equations that fit at least 99% of the variance in c_p at temperatures between 100 and 250 K:

$$c_p = 510.5 + 1.122T,$$
$$T > 150,$$
$$c_p = -0.14659T^2 + 42.104T - 2356.2,$$
$$T \leq 150$$

(3.2)

where *T* is in degrees Kelvin and c_p is in J K^{-1} kg^{-1}.

An example of a temperature profile with a convective instability and the lapse rates derived from it are shown in Figures 3.2a-b. The profile has a temperature maximum of 180 K at 30 Pa and may be unstable with respect to moist CO_2 convection near the surface. The large temperature error estimates above ~0.5 Pa are primarily due to the detector signal and noise being of comparable magnitudes when observing an atmosphere at exceptionally low temperature and pressure. Figure 3.2b shows that the lapse rate at ~0.4 Pa is clearly higher than the -4.5 K km^{-1} commonly quoted as the dry adiabatic lapse rate for the lower atmosphere, and it is also higher than the estimated dry adiabatic lapse rate. The difference between this lapse rate and the derived lapse rate is $\Gamma(p)$ and the $CAPE_{MA}$ due to this instability is ~232 J/kg. However, the instability is on the edge of the region where estimated temperature errors are becoming large, so the error in the estimate of $\Gamma(p)$ may be large as well. To estimate the error in $\Gamma(p)$ I generate 1000 random simulated realizations of the temperature profile based on the retrieval uncertainty using a Monte Carlo (MC) method driven by covariance data generated from
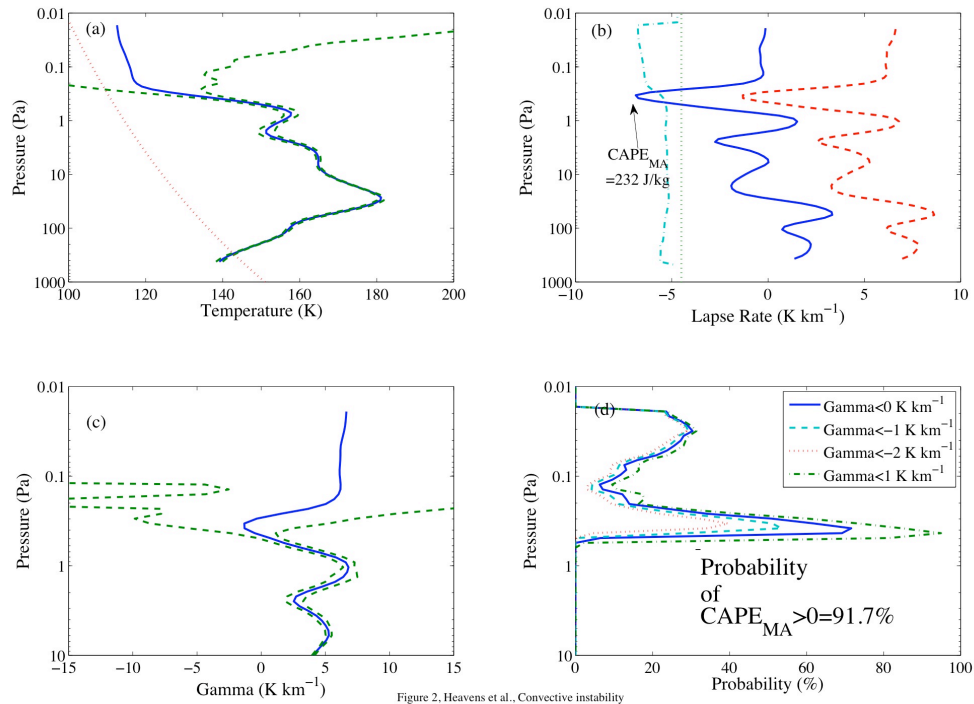
Figure 2, Heavens et al., Convective instability

Figure 3.2. (a) Example retrieved temperature profile with a dry instability (57° S, 89° E, L_s=125.3267, MY 28, 15:45 LST). Solid blue line shows temperature, $T(p)$, in K. Dashed green lines show 1-sigma error estimates for temperature. Dotted red line shows frost point of CO_2 based on algorithm of *Span and Wagner* [1996]; (b) solid blue line shows lapse rate for the retrieval in (a), dotted green line indicates constant lapse rate of -4.5 K km^{-1}, dot-dashed turquoise line shows variability in estimated dry adiabatic lapse rate with pressure, and dashed red line shows the estimated $\Gamma(p)$; (c) solid blue line shows estimated $\Gamma(p)$ from retrieval in (a) compared with 95% confidence intervals from the MC simulations; (d) Probability based on MC simulation of this profile that $\Gamma(p)$ is less than some particular threshold.

a representative sample of 1043 profiles: all of the dayside retrieved temperature profiles from 60° to 70° S, L_s=120°—130° of MY 29. $\Gamma(p)$ was calculated for each of the 1,000 MC realizations. In Figure 3.2c, $\Gamma(p)$ derived from the temperature profile is compared with the 95% confidence interval derived from the MC realizations (using the 26th and 975th lowest MC estimate of $\Gamma(p)$ at each pressure level). Like the temperature error, the divergence in the MC simulated $\Gamma(p)$ begins to grow at ~0.5 Pa. The probability of instability ($\Gamma(p) < 0$ K km^{-1}) exceeds 70% at ~0.5 Pa (Figure 3.2d), where the original profile was unstable. The extreme temperature uncertainties above 0.1 Pa (exceeding 80 K) create a secondary peak with a ~30% probability of instability. In this case, 91.7% of the realizations had a positive CAPE$_{MA}$. Statistically, this profile is only marginally unstable due to the retrieval uncertainties, although the region with the highest probability of instability does not correspond to the region of largest uncertainties.

Figure 3.3 shows the results of performing the Monte Carlo simulations on 2949 retrieved profiles. Instability thresholds of CAPE$_{MA} > 0$ J kg^{-1} and 50 J kg^{-1} were used to analyze both the retrieved and simulated profiles. For both thresholds, the cases where many of the simulated profiles exceed the threshold mostly correspond to retrieved profiles that are also unstable (Figures 3.3a and 3.3b). Fortunately, CAPE$_{MA}$ and the simulated probability of exceeding a particular CAPE$_{MA}$ threshold are linearly related (Figures 3.3c-d) when CAPE$_{MA} >$ ~50 J kg^{-1}. A small number of temperature profiles with derived CAPE$_{MA} >$ ~300 J kg^{-1} are unstable to 95% confidence (Figure 3.3c). Thus, we will call profiles with CAPE$_{MA} > 300$ J kg^{-1}, "significant instabilities." This linear relationship should hold for MCS temperature profiles in general. Figure 3.4 shows a
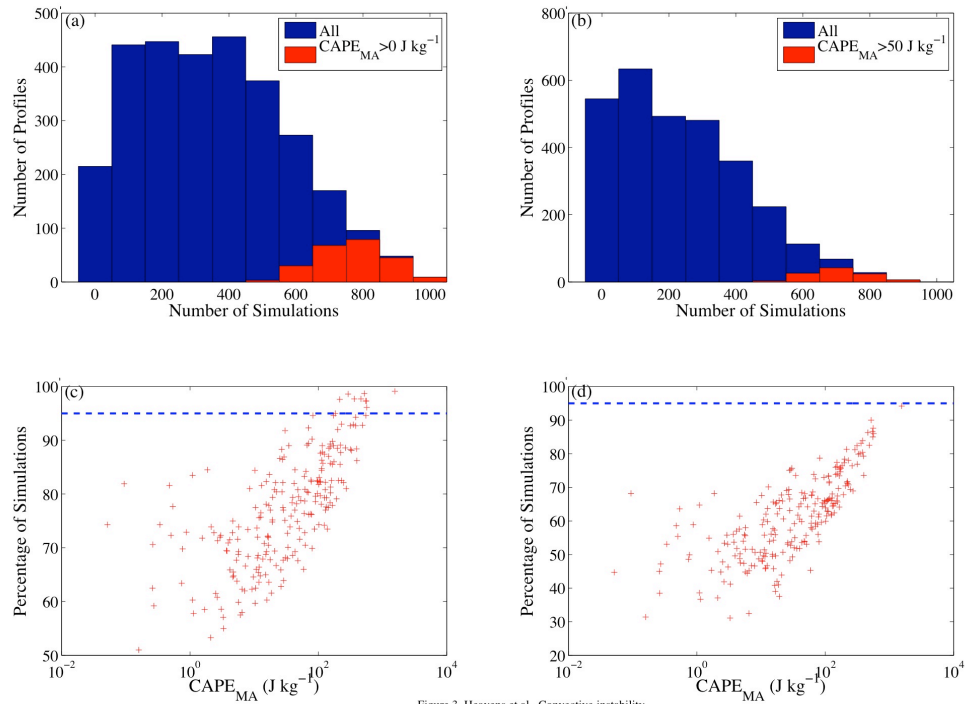
Figure 3, Heavens et al., Convective instability

Figure 3.3. Results of MC simulations of dayside retrievals from 60°-70° S, L_s=90°-120° of MY 29: (a) histogram of MC simulations with $CAPE_{MA}$>0 J kg^{-1} for all retrieved profiles and for all retrieved profiles with $CAPE_{MA}$ > 0 J kg^{-1}; (b) histogram of MC simulations with $CAPE_{MA}$ > 0 J kg^{-1} for all retrieved profiles and for retrievals with $CAPE_{MA}$ > 50 J kg^{-1}; (c) percentage of simulations with $CAPE_{MA}$ > 0 J kg^{-1} vs. derived $CAPE_{MA}$. The 95% confidence level is indicated with a blue dashed line; (d) percentage of simulations with $CAPE_{MA}$>50 J kg^{-1} vs. derived $CAPE_{MA}$. The 95% confidence level is indicated with a blue dashed line.

simple test of this idea, in which a temperature profile from near the north pole during

northern winter of MY 28 with CAPE$_{MA}$ of ~1000 J kg^{-1} is perturbed by +/- 2 times the

error estimate. A convective instability is present in both perturbed profiles, so the

instability is significant to at least 95% confidence as expected.

Inspection of this sample also shows that the isothermal condition imposed at the

top of the profile above the top detector weighting function [*Kleinböhl et al.*, 2009]

prevents unstable lapse rates from being derived where the temperature uncertainty

estimate is larger than ~8 K, so there is little justification to set an upper bound for

CAPE$_{MA}$ analysis.

The temperature profile in Figure 3.4 exemplifies the best-resolved convective

instabilities in MCS retrieved profiles. The unstable layer is ~5 km deep, the approximate

resolution of the retrieved profile, although it is embedded in a ~15 km deep region with

an enhanced lapse rate relative to most profiles below 10^{-1} Pa. The broad vertical retrieval

weighting functions smooth the retrieved temperature profile so that it poorly represents

the sharp temperature gradients of the instabilities. Convective instabilities must be

vertically extended and/or very strong to be detected in MCS profiles. Thus, this study

only provides a lower bound on the magnitude and distribution of convective instability

in the middle atmosphere.

3.2.3 Zonal Wind Estimates

For a necessary calculation in Chapter 3.4.2, we estimate the zonal gradient wind, $\tilde{U}(p)$.

This estimate is derived from the zonal average temperature by taking the lowest pressure
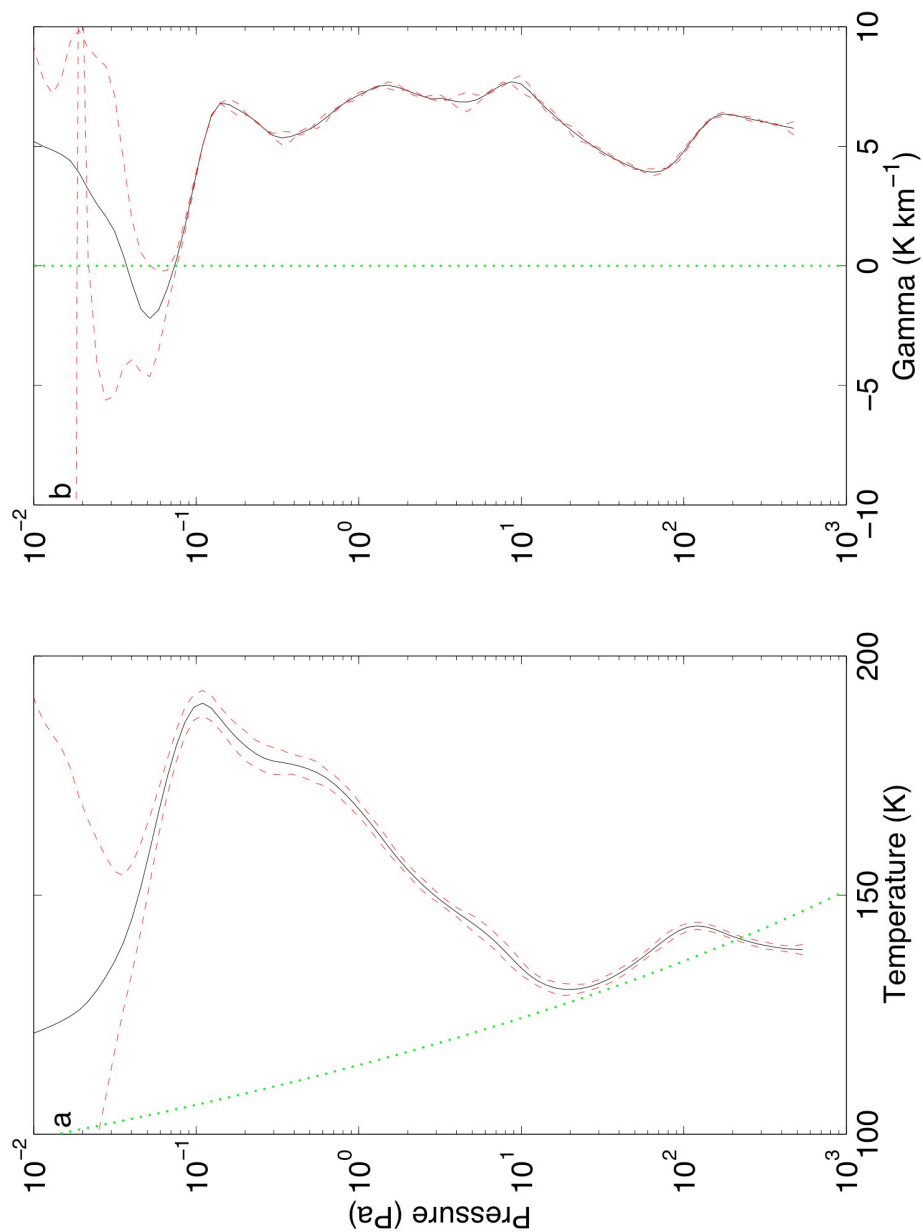
Figure 4, Heavens et al., Convective Instability

Figure 3.4. (a) Example retrieved temperature (K) profile with a dry instability (86° N, 160° W, L_s=265.1393, MY 28, 6:53 LST) with +/-2σ temperature error estimates (solid and dashed lines respectively). The dotted line indicates the CO_2 frost point; (b) $\Gamma(p)$ for the temperature profiles in (a). The dotted line indicates $\Gamma(p)$=0 K km^{-1}.

level with retrieved temperature data in each latitudinal bin as a level of no motion,

p_{LNM}, and estimating the thermal wind, $\hat{U}(p)$:

$$\hat{U}(p) = \int_{p_{LNM}}^{p} \frac{R_d}{f}\left(\frac{dT}{dy}\right)_p d\ln p' \tag{3.3}$$

where R_d is the specific gas constant, f is the Coriolis parameter for the latitudinal bin,

and $\left(\dfrac{dT}{dy}\right)_p$ is the temperature gradient at constant pressure. To compute the gradient wind

$\tilde{U}(p)$, we iteratively apply Eq. 3.4 to convergence [*Holton*, 2004].

$$\tilde{U}_{n+1}(p) = \frac{\tilde{U}_n}{1 + \dfrac{\sqrt{\tilde{U}_n^2}}{|fR_M|}} \tag{3.4}$$

where R_M is the radius of Mars. Eqs. 3.3 and 3.4 are only appropriate for winds in

approximate geostrophic balance and so cannot be used for diagnosis of zonal winds in

the tropics due to the low magnitude of the Coriolis parameter. Therefore, $\tilde{U}(p)$

calculated in the tropics is not plotted.

3.3 Results

3.3.1 Global Results

Figures 3.5a-b show example nightside and dayside zonal averages of $T(p)$ at northern

summer solstice in which polar middle atmospheric temperature maxima of ~180 K are

observed at a pressure level of ~1-2 Pa (~40-50 km above the local surface) in the high
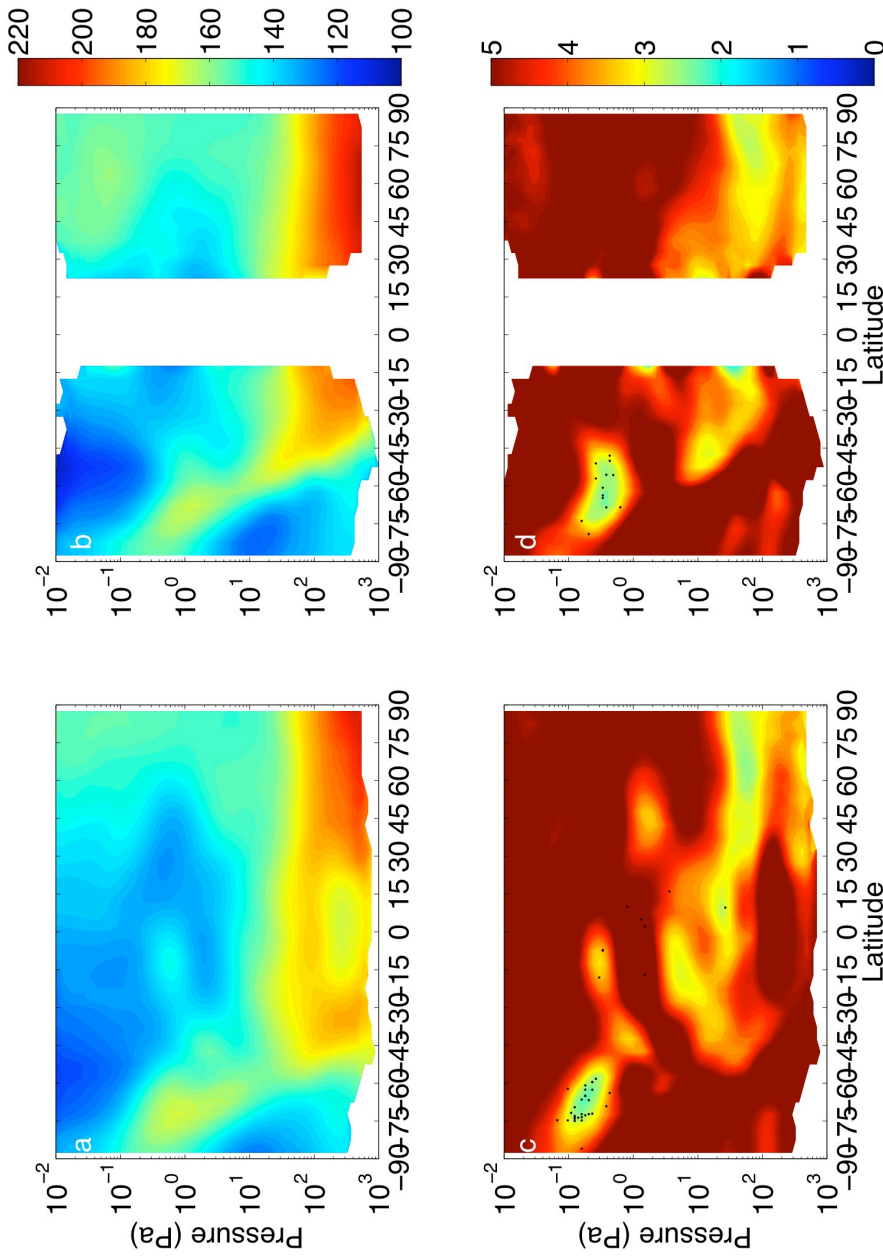
southern latitudes.

Figure 5, Heavens et al., Convective Instability

Figure 3.5. (a) zonal average of $T(p)$ (K), MY 29, $L_s=87.5°$-$92.5°$, nightside; (b) zonal average of $T(p)$ (K), MY 29, $L_s=87.5°$-$92.5°$, dayside; (c) zonal average of $\Gamma(p)$ (K km^{-1}), MY 29, $L_s=87.5°$-$92.5°$, nightside. (d) Zonal average of $\Gamma(p)$, MY 29, $L_s=87.5°$-$92.5°$, dayside. The color scale for $\Gamma(p)$ is saturated at 5 K km^{-1} to de-emphasize positive lapse rates. Missing data is indicated in white. Black dots in (c) and (d) mark the locations of the minimum $\Gamma(p)$ of significant instabilities.

Figures 3.5c-d show zonal average $\Gamma(p)$ during the same L_s range and the pressures at which individual profiles with $CAPE_{MA} > 300$ J kg^{-1} are most unstable (the locations of significant instabilities). The zonal average structure is not unstable anywhere, but very low values of $\Gamma(p)$ and the densest concentration of significant instabilities are at ~0.3 Pa (~60 km above the local surface) from 50° S nearly to the pole. Only lapse rates in the lower atmosphere near the north pole are comparably close to the dry adiabatic lapse rate. The southern zone of low stability lies ~2 scale heights directly above the polar warming described by *McCleese et al.* [2008] (and seen in Figures 3.5a-b). There is a middle atmospheric temperature maximum of ~160 K at very low pressures over the north pole, but lapse rates over this region appear more stable.

In a few cases on the nightside, significant instabilities occur at ~3 Pa over the tropics in a region of the atmosphere that is on the average very stable (Figure 3.5c). Inspection suggests these instabilities are artifacts of retrieval through high hazes. In this particular case, there are sufficient profiles in the same longitudinal bin such that the zonal average lapse rate is far from adiabatic and zonal average $CAPE_{MA}$ is low, but care must be taken at other seasons.

Figures 3.6a-f show how $CAPE_{MA}$ is distributed among individual profiles in single latitudinal bins. In the latitude/L_s bins whose distributions are depicted in Figures 3.6a-d and 3.6f, the fraction of profiles with $CAPE_{MA}$ in a given $CAPE_{MA}$ interval decreases with increasing $CAPE_{MA}$. The distribution and zonal average $CAPE_{MA}$ for each of these bins is consistent and physically plausible. The distribution in Figure 3.6e is different. It is flat, and the average is much higher than expected. One of the high
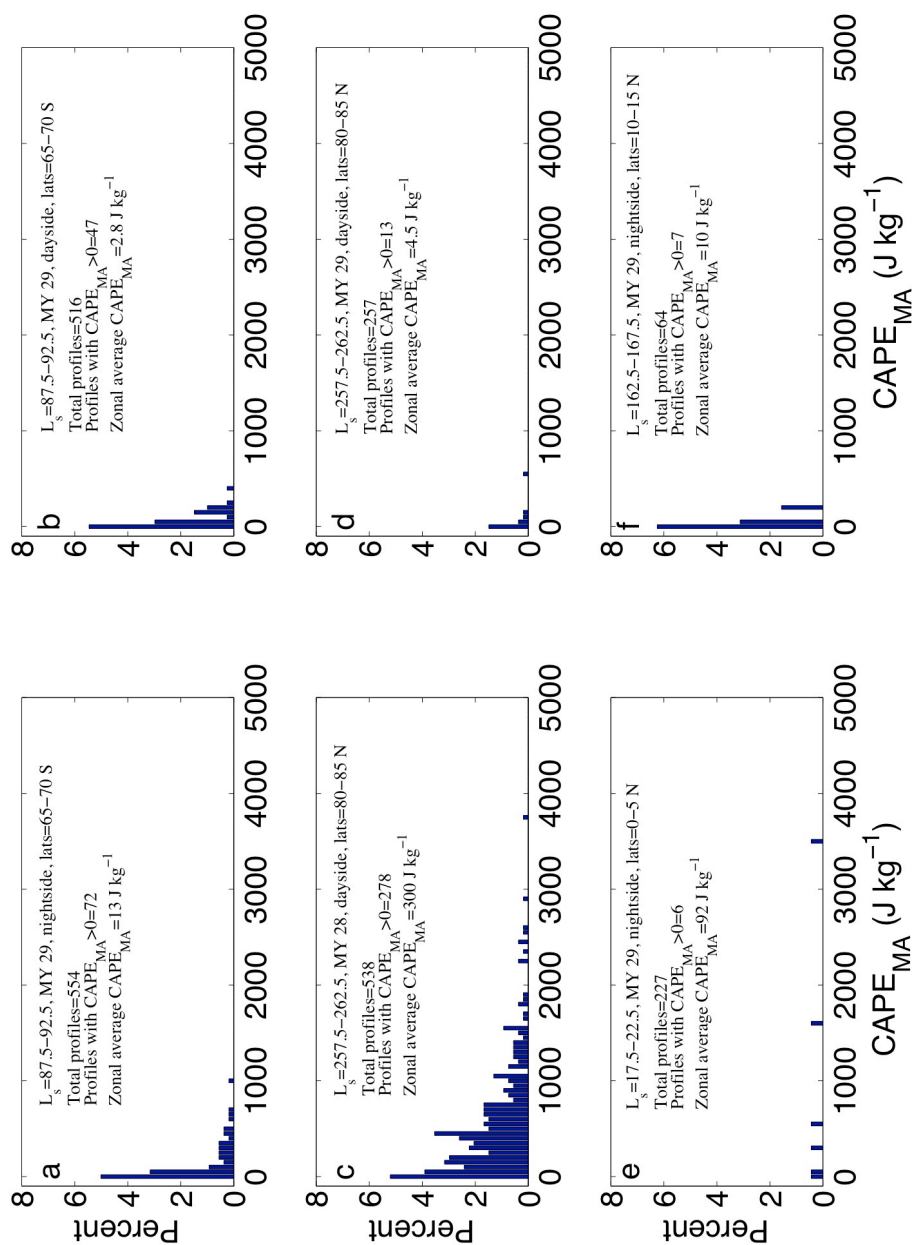
Figure 6, Heavens et al., Convective Instability

Figure 3.6. (a) Histogram of CAPE$_{MA}$ (50 J kg^{-1} binning resolution) in individual profiles from six different L$_s$/latitudinal bins. See captions within figure for details.

$CAPE_{MA}$ profiles is the only one in its longitude bin, heavily weighting the mean. An inspection indicates the presence of a high haze.

In order to eliminate such artifacts, the zonal average $CAPE_{MA}$ is filtered with two binomial one-tailed tests at 95% confidence with the null hypotheses: (1) the fraction of profiles $CAPE_{MA} > 0$ J kg^{-1} is random, assuming the ordinary probability is the fraction of profiles meeting this criterion in the dataset (2.92%); (2) the fraction of profiles 0 J kg^{-1} < $CAPE_{MA} < 50$ J kg^{-1} is random, assuming the ordinary probability is the fraction of profiles meeting this criterion in the dataset (1.44%). Latitude/L_s bins with high $CAPE_{MA}$ typically pass (1), but if the distribution is similar to Figure 3.6e, it will not pass (2). These tests should not be considered statistically rigorous but only as an empirical filter to direct attention from occurrences of instability attributable to high hazes.

Figures 3.7, 3.8 and 3.9 show the minimum zonal mean $\Gamma(p < 50$ Pa), the pressure at which it occurs, and the filtered zonal average $CAPE_{MA}$ over the seasons. They provide an overview of middle atmospheric convective instabilities in the MCS retrieved profiles and the zonal average stability structure. During most of the spring and summer, the lowest values of $\Gamma(p)$ in the extratropics are at pressures greater than 50 Pa (Figure 3.7). While nightside average lapse rates in the northern extratropics can be relatively high during northern spring and summer, lapse rates in individual profiles remain sub-adiabatic, and zonal average $CAPE_{MA}$ is below 1 J kg^{-1}.

In the southern extratropics during the same season (its fall and winter), the situation is very different. Zonal average $CAPE_{MA}$ can be up to 100 J kg^{-1} on both the dayside and nightside. The minimum $\Gamma(p < 50$ Pa) is at $p < 1$ Pa and is ~10 km higher on
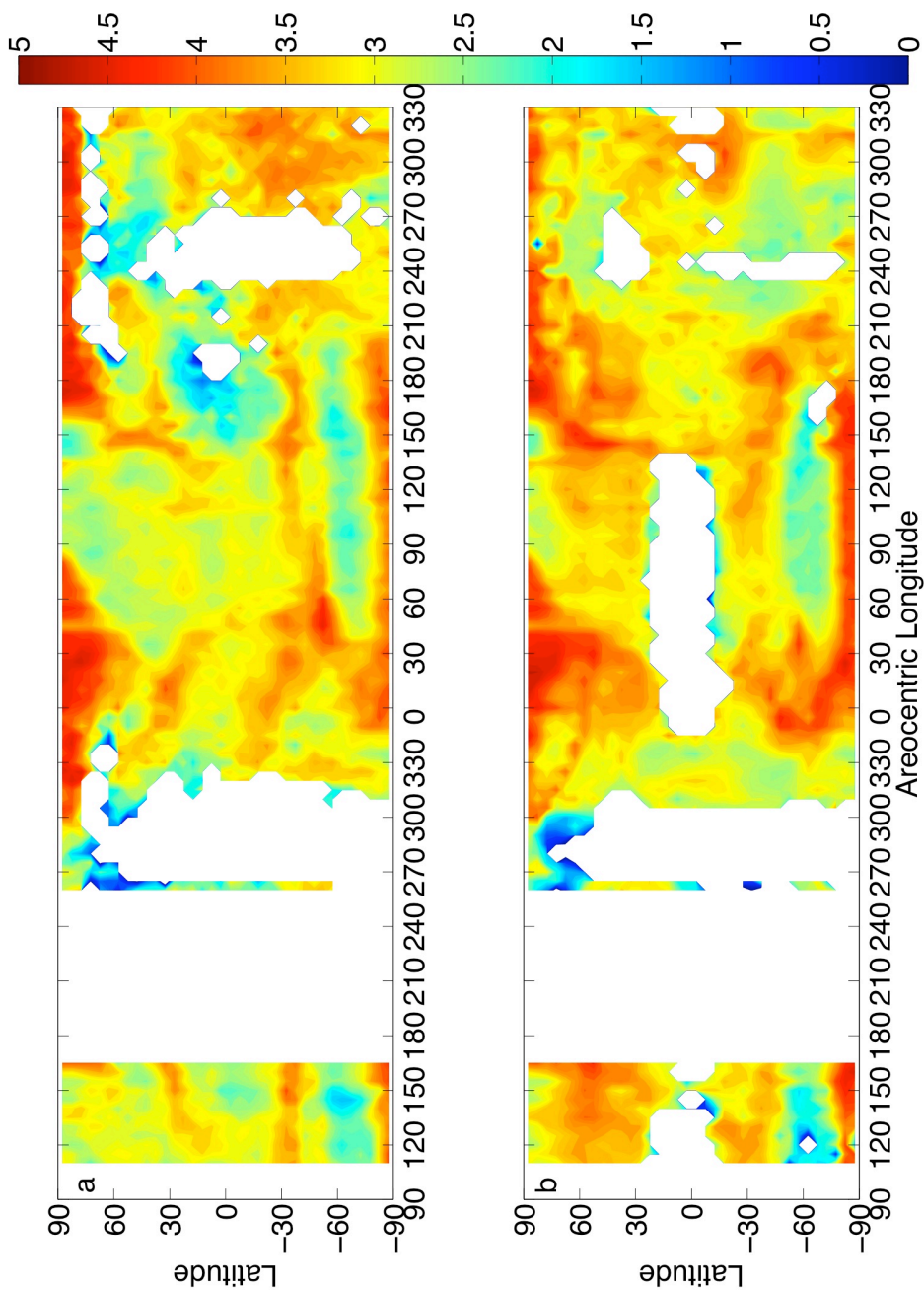
Figure 7, Heavens et al., Convective Instability

Figure 3.7. Latitudinal and seasonal variability during MY 28 and 29 in the minimum zonal average $\Gamma(p <$ 50 Pa) (K km^{-1}) using retrieved profiles from limb scanning data only: (a) nightside; (b) dayside; The color scale for those plots is saturated at 0 and 5 K to emphasize marginally unstable lapse rates. White space represents L$_s$/latitudinal bins without retrieved profiles from limb scanning data.
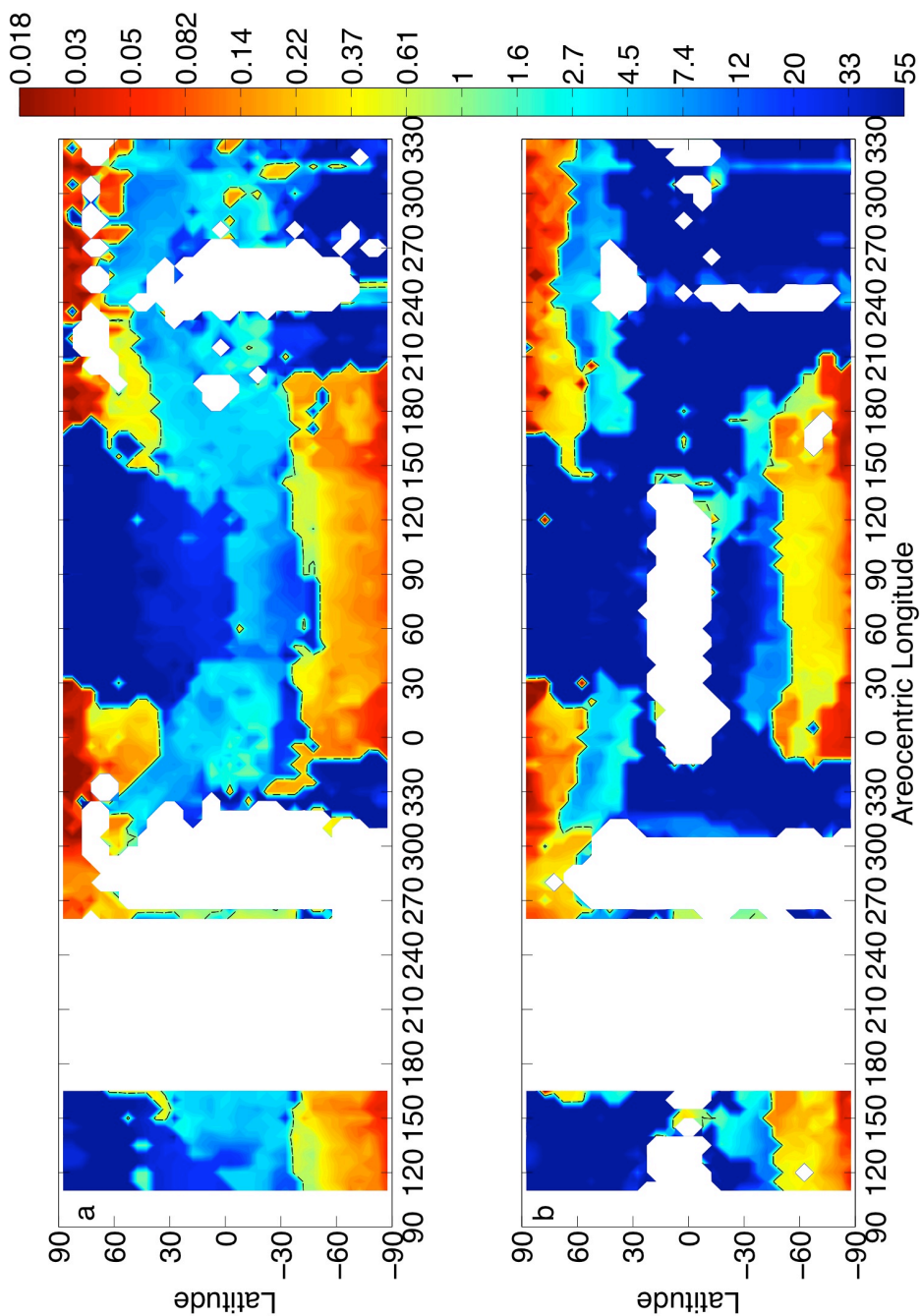
Figure 3.8. Latitudinal and seasonal variability during MY 28 and 29 in the pressure (Pa) at which the minimum zonal average $\Gamma(p < 50$ Pa) is observed using retrieved profiles from limb scanning data only: (a) nightside; (b) dayside. The dashed black line is the 1 Pa contour. White space represents L_s/latitudinal bins without retrieved profiles from limb scanning data.
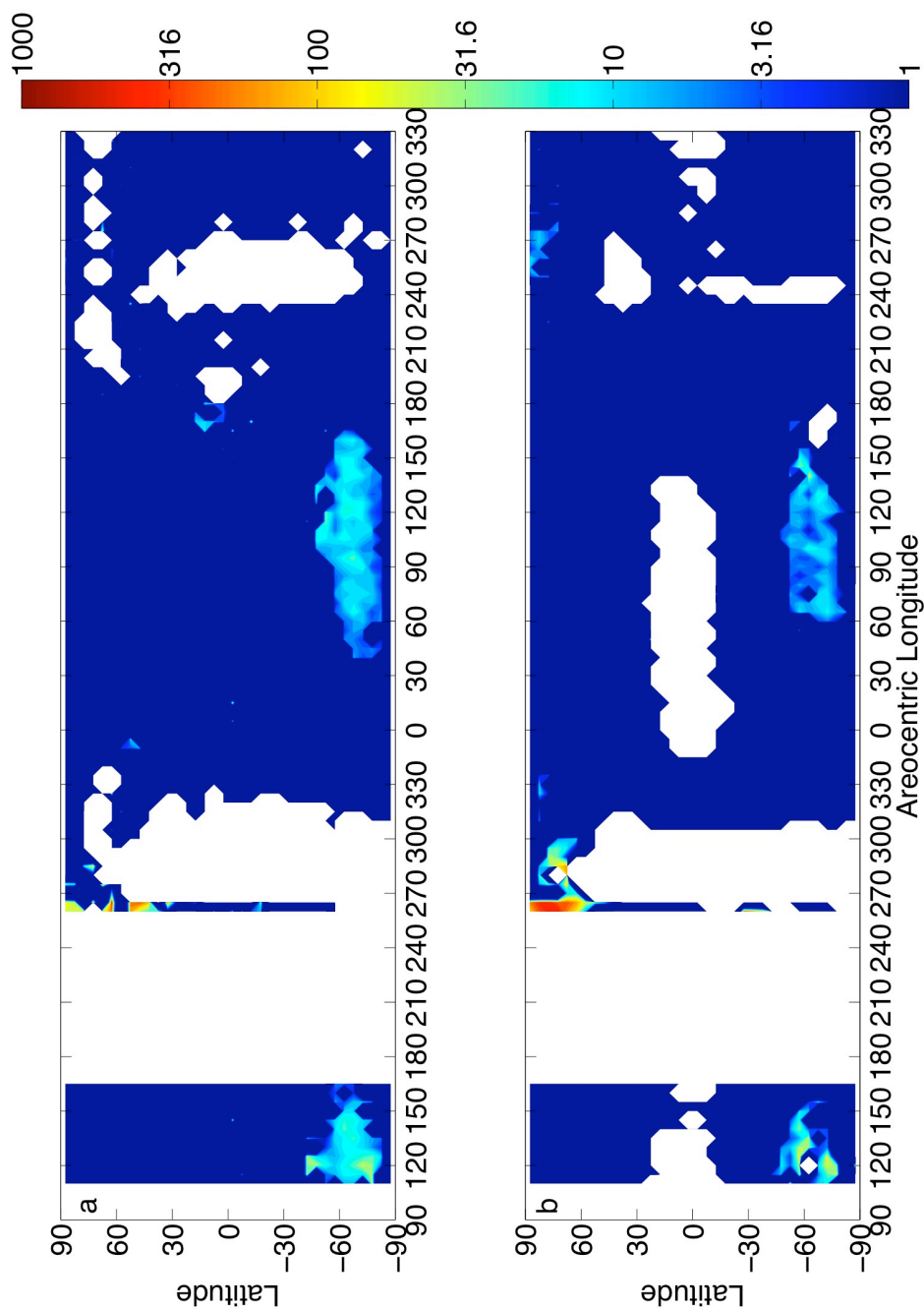
Figure 3.9. Latitudinal and seasonal variability during MY 28 and 29 in CAPE$_{MA}$ (J kg^{-1}) using retrieved profiles from limb scanning data only and filtered as described in the text: (a) nightside; (b) dayside. The color scale is log$_{10}$ and saturates below 1 J kg^{-1}. White space represents L$_s$/latitudinal bins without retrieved profiles from limb scanning data.

the nightside than the dayside (also see Figures 3.5c and 3.5d). The lowest values of Γ

(p) are generally between 1.5 and 2.5 K km^{-1} but are as low as 0.2 K km^{-1} on the dayside

between 60° and 65° S at L_s=125° of MY 28 (Figure 3.7). The extremely low zonal

average $\Gamma(p)$ at this latitude and season is most likely an underestimate due to poor

sampling, in which only unstable perturbations of the mean stability structure are

sampled. Only four longitudinal bins include retrievals (one in each bin). After

accounting for the limitation in available data, interannual variability between MY 28 and

MY 29 appears weak during this season.

In the northern extratropics during its fall and winter, zonal average $\Gamma(p)$ has a

minimum at ~0.1 Pa and is in fact unstable at poorly sampled latitudes (12 longitudinal

bins) at L_s=260° of MY 28. At better-sampled latitudes (58 longitudinal bins), the lowest

zonal average $\Gamma(p)$ at this time is ~ 1 K km^{-1}, a large number of unstable layers in

individual profiles are within this zone of low mean stability (Figure 3.10a), and zonal

average CAPE$_{MA}$ is up to 500 J kg^{-1}. (Figures 3.10a-f have a similar format to Figures

3.5c-d to illustrate the full mean stability structure of the atmosphere and the location of

the most unstable layers in individual profiles.) Note that both $\Gamma(p)$ and zonal average

CAPE$_{MA}$ in the northern extratropics differ significantly between MY 28 and MY 29. We

will investigate this interannual variability in greater detail in Chapter 3.3.2.

In the tropics, $\Gamma(p)$ usually has a weak minimum (greater than ~3 K km^{-1})

between 1 and 30 Pa. During late northern summer and early northern fall, $\Gamma(p)$ is as low

as ~1 K km^{-1}. Zonal average CAPE$_{MA}$ in the tropics is less than 1 J kg^{-1}, except for one

small nightside region at L_s ~180°. This CAPE$_{MA}$ is mostly contributed by marginally

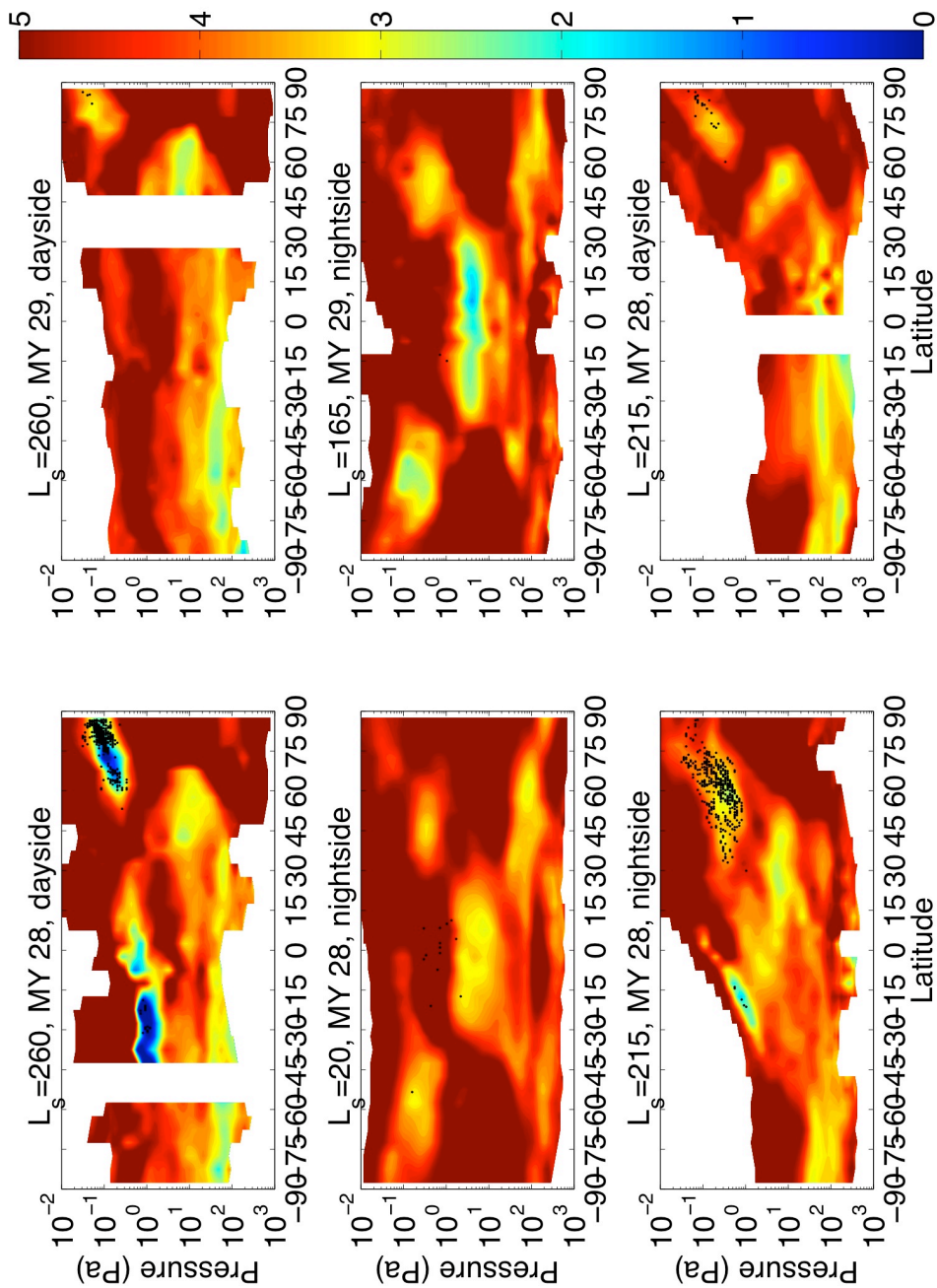unstable layers in individual profiles within a zone of low mean stability at ~5 Pa (Figure

Figure 3.10. Zonal average of $\Gamma(p)$ (K km^{-1}). Black dots mark the locations of the minimum $\Gamma(p)$ of significant instabilities. The color scale for $\Gamma(p)$ is saturated at 5 K km^{-1} to de-emphasize positive lapse rates. Missing data is indicated in white.

3.10d). The biggest impact of our empirical filter is during $L_s=0°-30°$ of MY 29; without it, zonal average $CAPE_{MA}$ is as high as 100 J kg^{-1} on the nightside because of retrievals through high hazes. These appear as significant instabilities in otherwise stable regions in the zonal average (Figure 3.10c).

3.3.2 Convective Instability in the Northern Extratropics

Zonal average $CAPE_{MA}$ was much higher during MY 28 than in MY 29 from $L_s=180°$ to 280°: ~100—500 J kg^{-1} in MY 28 but only 1-10 J kg^{-1} during MY 29 (Figures 3.13a-b). $CAPE_{MA}$ also was higher during this year, season, and latitudinal band than it was in the southern extratropics during southern fall and winter. (Note the inclusion of retrieved temperature profiles from limb staring data.) The distribution of $CAPE_{MA}$ in individual profiles (Figures 3.6c-d) and the mean stability structure between the two years clearly differ as well (Figures 3.10a-b) at $L_s=260°$, the peak of instability during MY 28.

During MY 28, significant convective instabilities were widespread in the northern extratropics from northern fall equinox but were reduced to levels lower than those in southern hemisphere winter after $L_s=266°$ (Figures 3.11a-b). A global dust storm began around $L_s=261.5°$ of MY 28 (results presented by B.A. Cantor et al., Observations of the Martian Atmosphere by MRO-MARCI: An Overview of 1 Mars Year, Third International Workshop on Mars Modeling and Observations, Lunar and Planetary Institute, Williamsburg, VA, 10-13 November 2008), so the convective instability was suppressed ~7 sols after the beginning of the dust storm. The suppression is roughly synchronous with the initial polar vortex displacement and breakdown due to this storm described by D.M. Kass et al. (MCS Views of the 2007 Global Dust Storm, paper
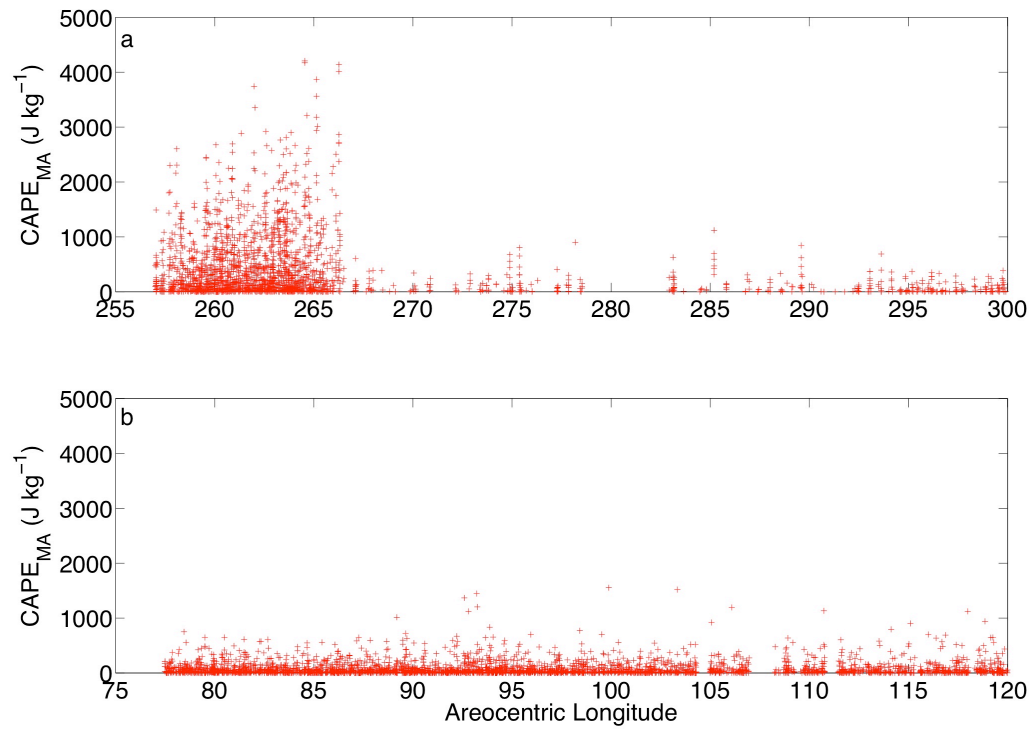
Figure 11, Heavens et al., Convective Instability

Figure 3.11. (a) $CAPE_{MA}$ in individual profiles with latitudes north of 60°N vs. L_s in MY 28, L_s=257°—

300°; (b) $CAPE_{MA}$ in individual profiles with latitudes south of 60°S vs. L_s, MY 29, L_s=77°—120°.
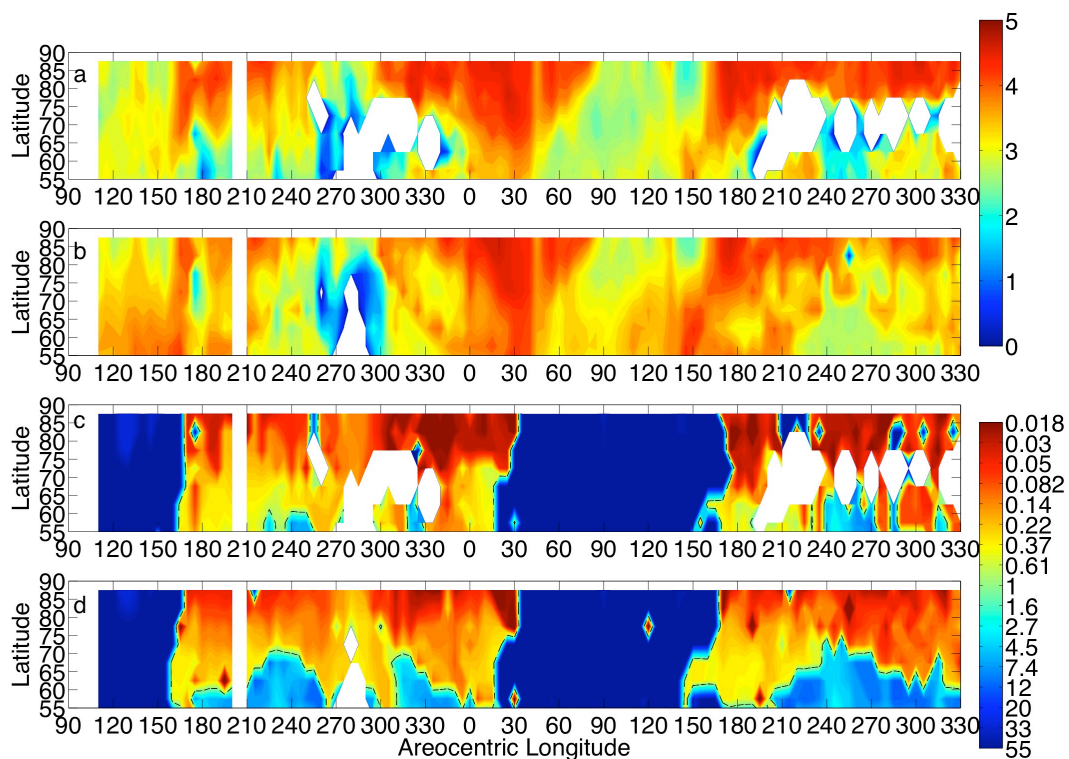
Figure 12, Heavens et al., Convective Instability

Figure 3.12. Latitudinal and seasonal variability during MY 28 and 29 in the minimum zonal average $\Gamma(p < 50$ Pa) (K km^{-1}) and the pressure (Pa) at which it occurs using retrieved profiles from both limb staring and limb scanning data: (a) $\Gamma(p < 50$ Pa), nightside; (b) $\Gamma(p < 50$ Pa), dayside; (c) pressure of occurrence for (a); (d) pressure of occurrence for (b). Only latitudes north of 55° N are shown as discussed in the text.
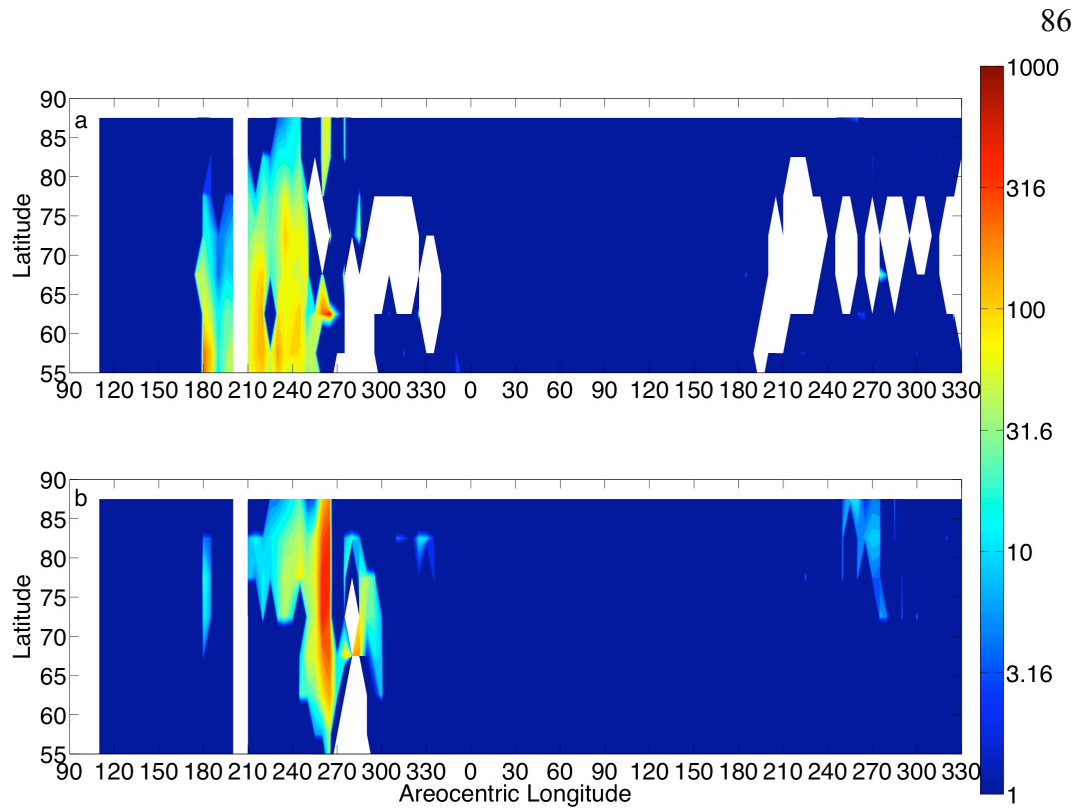
Figure 13, Heavens et al., Convective Instability

Figure 3.13. Latitudinal and seasonal variability during MY 28 and 29 in the zonal average $CAPE_{MA}$

(J kg^{-1}) using retrieved profiles from both limb staring and limb-scanning data: (a) nightside; (b) dayside.

Only latitudes north of 55° N are shown as discussed in the text.

presented at the 39th Meeting of the Division for Planetary Sciences of the American

Astronomical Society, Orlando, FL, 7-12 October 2007). There is strong dayside-

nightside variability in $CAPE_{MA}$ between 55º and 70º N during L_s=180°-260° of MY 28

(Figures 3.13a-b). The least stable average lapse rates occur at $p > 1$ Pa at this latitudinal

band and season during both MY 28 and MY 29 (Figures 3.12a-d). Figures 3.10e-f show

this dayside-nightside variability is connected to changes in the width of a zone of low

mean stability at ~0.3 Pa in the northern extratropics. Significant instabilities in

individual profiles are present on the nightside, but not on the dayside during MY 28.

Neither the zone of low mean stability at ~10 Pa in the northern tropics/mid-latitudes, nor

the poleward extension on the dayside contain profiles with significant instabilities. Thus,

whatever phenomenon is generating the instability in this latitudinal band and season

during MY 28 could generate it within a zone of low mean stability at ~0.3 Pa but not

within a zone of low mean stability at ~10 Pa. The existence of a zone of low mean

stability at ~0.3 Pa at this latitudinal band and season during MY 29 without significant

$CAPE_{MA}$ may imply that whatever phenomenon was generating the instability during MY

28 was weaker during MY 29.

3.4 Discussion

3.4.1 Interpretation of Middle Atmospheric Convective Instabilities

We propose that the convective instabilities described in Chapters 3.2 and 3.3 are the

result of gravity wave saturation modulated by the thermal tides. (The diurnal tide is

particularly apparent in MCS observations, but modeling suggests the semi-diurnal tide may be equally or more important during large-scale dust storm activity [*Forbes and Miyahara*, 2006]). Above the tidal anti-nodes, there are regions of lower stability with respect to the mean thermal structure. (In the case of pure tidal breakdown, these regions actually would be convectively unstable.) An internal gravity wave has a warm phase and a cold phase in the vertical. The boundary between the warm and the cold phase is a perturbation toward instability. Thus, if the unstable phase of an internal gravity wave propagates through a region of low stability due to the tide and/or the mean thermal structure, a convective instability may be created. As the tidal anti-nodes move up and down during the course of the day, the level of gravity wave saturation will change. In this way, the tides can modulate where gravity wave saturation occurs without being unstable on their own.

Tidal modulation is evident in Figures 3.5a and 3.5b, which show a strong vertically propagating tidal anti-node centered at 15° S at a level of 0.7 Pa on the nightside that rises to 0.07 Pa on the dayside. In Figure 3.5c, this anti-node is associated with a local minimum in $\Gamma(p)$ near which occur significant instabilities in two individual profiles. The region of low stability at 65° S at ~0.3 Pa on the nightside is lower on the dayside due to the influence of the tide. The tide appears to be defining the sharpness of the top of the middle atmospheric temperature maximum [*McCleese et al.*, 2007; *Lee et al.*, 2009]. There is similar day-night variability in the stability structure in middle of northern fall of MY 28 (Figures 3.10e-f).

The observed variability in stability, however, does not appear consistent with pure tidal breakdown. Away from the poles, MCS observes at approximately the same

local time (and thus same tidal phase). In the case of pure tidal breakdown, we would expect the zonal average $\Gamma(p)$ for nightside or dayside to be unstable. There indeed are instances of unstable zonal average $\Gamma(p)$, but these instances are in bins with longitudinal sampling no greater than 20%. Where longitudinal sampling is complete, the minimum zonal average $\Gamma(p)$ is always greater than 1.5 K km^{-1}, requiring a significant additional perturbation to explain the unstable lapse rates in individual profiles.

A plausible case in which gravity waves may have destabilized portions of the atmosphere already close to neutral stability is illustrated in Figures 3.14a-d. Figures 3.14a-c show longitudinal cross-sections of $\Gamma(p)$ in individual profiles along an orbit. Figure 3.14d illustrates the zonal average $\Gamma(p)$ on both the dayside and nightside. At this latitude, the instrument is looking more westward than northward or southward and thus its observations broadly integrate over a range of local times centered at ~4:30 LST on the nightside and ~13:00 LST on the dayside. While there is some diurnal variability (not necessarily tidal in origin), the mean atmosphere on both the dayside and nightside is highly stable (lapse rates more stable than isothermal) between 50 and 0.2 Pa and near neutral stability (lapse rates less stable than isothermal) between 0.2 and 0.02 Pa.

Figures 3.14a-c show several examples of smaller-scale perturbations in $\Gamma(p)$ that are coherent between profiles within the broad layer of near-neutral stability. For instance, Figure 3.14b shows a nearly isothermal perturbation at ~0.5 Pa, a highly stable perturbation at ~0.25 Pa, and an unstable perturbation at ~0.06 Pa. If these perturbations were gravity waves propagating vertically, their vertical and horizontal wavelengths would be ~10 and ~150 km respectively.
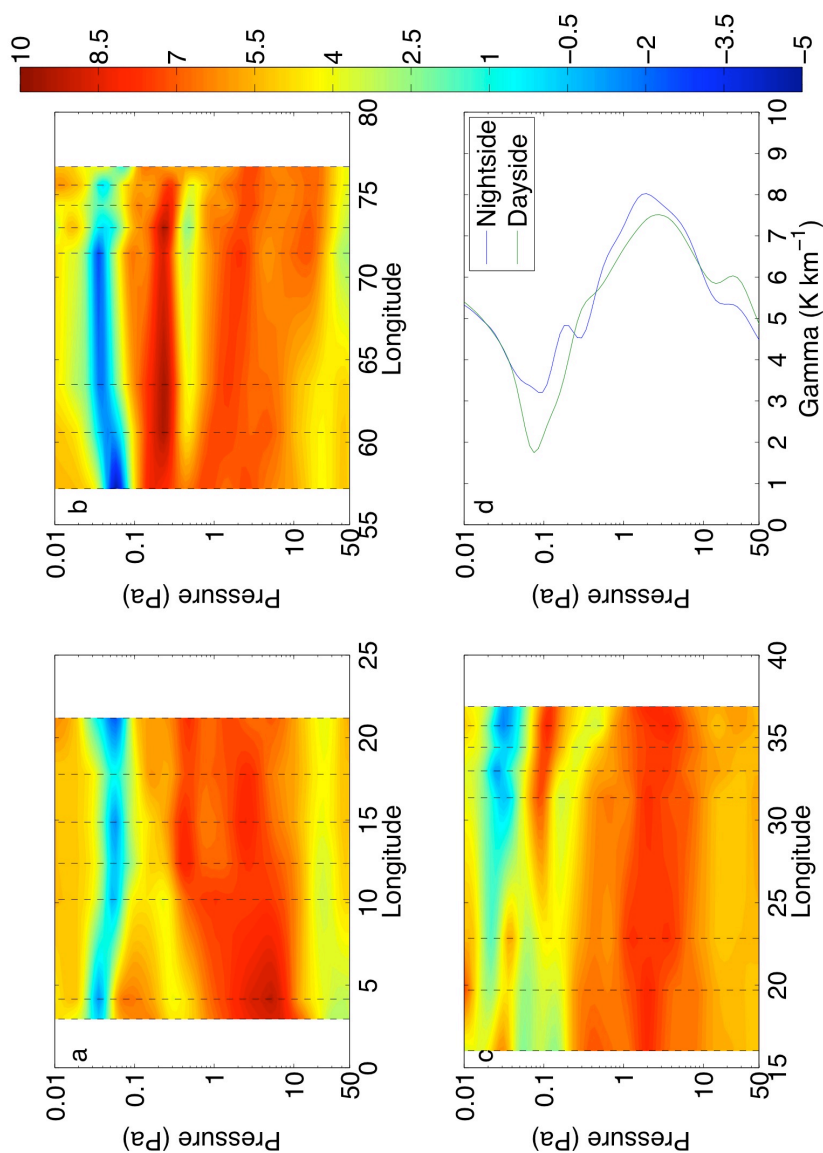
Figure 3.14. Cross-sections of $\Gamma(p)$ constructed from individual profiles retrieved from observations during northern fall of MY 28 near the north pole: (a) orbit number 4177 (17 June 2007), latitudes=80.6369°—84.8568° N, L_s= 259.5701°—257.5707°, 4:12—5:24 LST; (b) orbit number 4140 (15 June 2007), latitudes=80.0047°—84.7466° N, L_s= 257.7412°—257.7419°, 12:27-13:43 LST; (c) orbit number 4181 (18 June 2007), latitudes=80.2689°—84.9621° N, L_s= 259.7657°—259.7664°, 12:17—13:39 LST; (d) zonal average $\Gamma(p)$, MY 28, L_s=257.5°—262.5°. The black dashed lines in the cross-sections indicate the mean longitudes of the profiles. Breaks in spacing likely indicate where retrieval was unsuccessful.

Even in the absence of the perturbations, pure tidal breakdown would be an unlikely

explanation for the instabilities at this latitude and season. On the dayside, about half of

the profiles have $CAPE_{MA} > 0$ (Figure 3.6c), but the minimum zonal average $\Gamma(p)$ is

1.7 K km^{-1}. Thus, for every perturbation toward instability within the region of near-

neutral stability, there should be (and inspection suggests it) a perturbation toward high

stability, as would be expected for a region experiencing a high flux of vertically

propagating gravity waves with randomly distributed phases. The coherent structures

seen in Figures 3.14a-c are not easily identified at other latitudes and seasons, where

instabilities are far less common, but we suspect that the convective instabilities observed

elsewhere in the middle atmosphere are caused by the same mechanism.

3.4.2 Dynamical Significance

The primary effect gravity waves and tides have on the circulation can be described by

the zonal momentum equation as in *Barnes* [1990]:

$$\frac{\partial \overline{U}}{\partial t} - f\overline{V} = F_x + \frac{\partial}{\partial z}\left(D\frac{\partial \overline{U}}{\partial z}\right) \qquad (3.5)$$

where $\overline{U}$ and $\overline{V}$ are the mean zonal and meridional winds, F_x is the zonal wave drag, and

D is a diffusion constant. Modeling shows that the westerly jets tend to be stabilized in

the presence of wave drag by enhancement of the mean meridional flow toward the pole

and downwelling, as implied by the second left hand side term of Eq. 3.5. At least to first

order, the major difference between wave drag due to gravity waves and tides is their

differing phase speeds. Gravity waves have low or stationary phase speeds typical of

lower atmospheric winds, while sun-synchronous tides have a phase speed that matches

the planetary rotation speed at the latitude at which they propagate [*Lindzen*, 1981].

Thus, gravity waves and tides usually accelerate the mean flow in different ways.

Because we interpret the convective instabilities (and thus dissipation) to result primarily

from gravity waves, we will focus on the wave drag due to gravity waves alone.

F_x can be defined in terms of the vertical convergence of the momentum flux in

the x-direction:

$$F_x = -\frac{1}{\rho}\frac{\partial}{\partial z}\left(\rho\langle u'w'\rangle\right)$$
(3.6)

where ρ is the density and $\langle u'w'\rangle$ is the zonal momentum flux of the gravity waves. The

key observational constraint for modeling the effect of gravity waves on the martian

circulation then would be an estimate of the zonal momentum flux. Because MCS is

probably most sensitive to meridionally propagating waves, the gravity wave saturation

detected may be primarily a source of meridional rather than zonal momentum to the

circulation. So we will focus on estimating the drag due to the inferred saturating waves

in Figure 3.14, a case in which MCS may be more sensitive to zonally propagating

waves.

To estimate the wave drag, I adopt the drag parameterization of *Barnes* [1990]:

$$F_x = \frac{-\gamma k_h(\overline{U}-c)^3}{N}\left[\frac{1}{2H} - \frac{3\frac{d\overline{U}}{dz}}{2(\overline{U}-c)}\right]$$
(3.7)

where γ is a parameter called the "intermittency factor," k_h is the horizontal wavenumber

of the waves, and H is the scale height. Note that Eq. 3.7 is evaluated at the level of

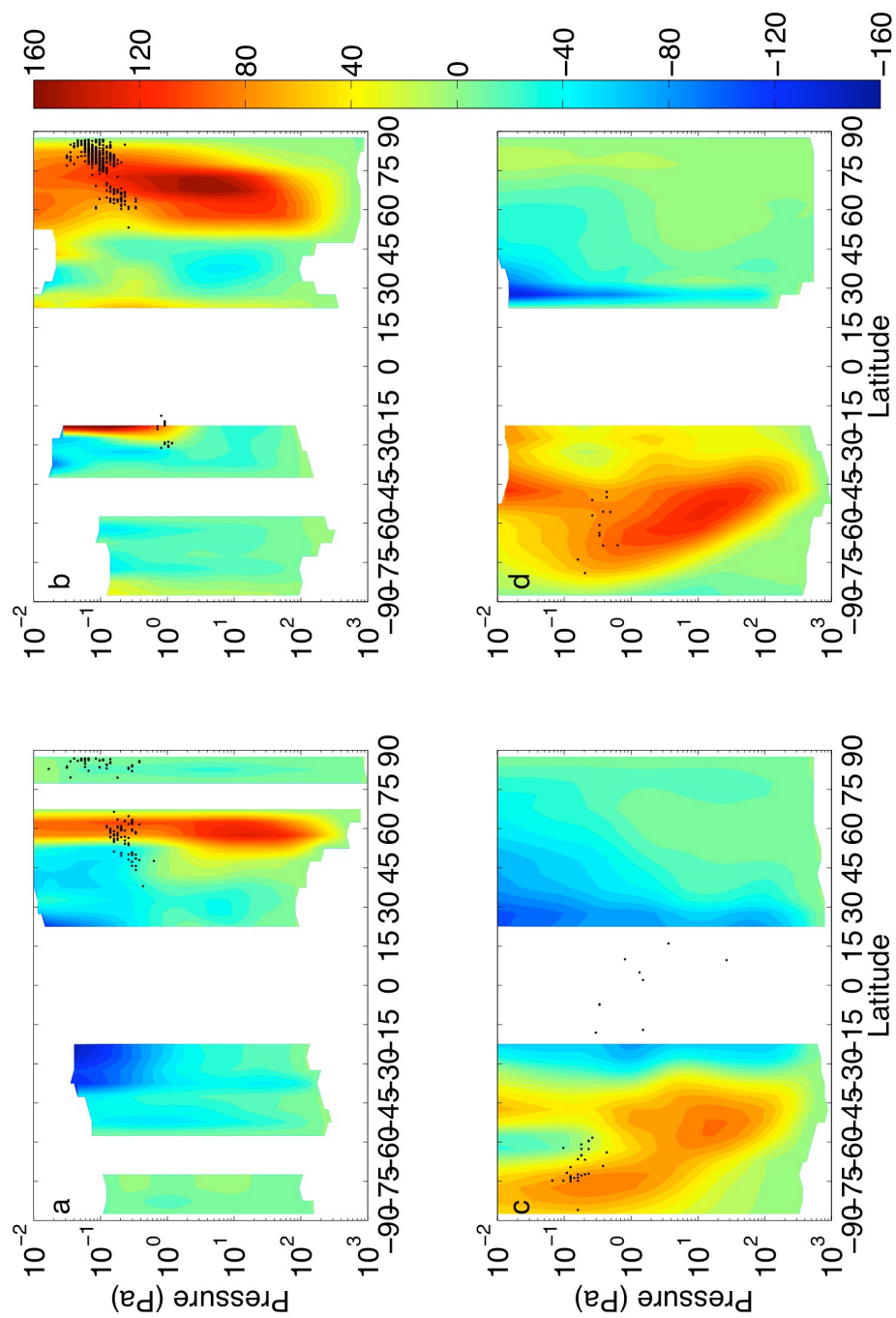**Figure 3.15.** Estimated zonal gradient wind, $\tilde{U}(p)$ (ms^{-1}) for: (a) L$_s$=260°, MY 28, nightside; (b) L$_s$=260°, MY 28, dayside; (c) L$_s$=90°, MY 29, nightside; (d) L$_s$=90°, MY 29, dayside.

Figure 15, Heavens et al., Convective Instability

gravity wave breaking. As a guide to estimate $\overline{U}$ and $\dfrac{d\overline{U}}{dz}$, Figures 3.15a-d show the

estimated zonal gradient wind, $\tilde{U}$, for nightside and dayside of L_s=260° during MY 28

and L_s=90° durinMY 29 along with the locations of the most unstable profiles, just as in

Figures 3.5 and 3.10.

Let us then consider a stationary wave (c=0) with k_h=4×10^{-5} m^{-1} (a horizontal

wavelength of ~150 km) in a mean zonal wind of 75 ms^{-1} (the estimated dayside zonal

wind at 10^{-1} Pa at 80°—85° N in Figure 3.15b) with N=10^{-2} s^{-1}, and H=8,000 m. The

vertical wind shear, $\dfrac{d\overline{U}}{dz}$, is ~2×10^{-4} s^{-1} at the same pressure level and latitude/L_s bin.

Fritts and Alexander [2003] says that the intermittency factor, "can be thought of as

describing the fractional coverage of the wave dissipation event within the larger scale

space- and/or time-averaging interval." One simple and perhaps overly generous estimate

of the intermittency factor is the fraction of profiles in the zonal averaging bin that

contain instabilities, which is 0.52 for the dayside of L_s=260° during MY 28 (Figure

3.6c). (In general, we expect the intermittency factor to be directly but not necessarily

linearly proportional to average CAPE$_{MA}$.) In that case, F_x=-0.05 ms^{-2} or

-4,500 ms^{-1} sol^{-1}. If waves of similar horizontal wavelength are creating the instabilities

in the southern extratropics, drag there during southern fall and winter may be an order of

magnitude weaker, since zonal average CAPE$_{MA}$ and the proportion of unstable profiles

is around an order of magnitude lower. The zonal winds in the region of breaking are

similar, though they are generally faster in the northern extratropics.

The estimated drag in the northern extratropics before the 2007 global dust storm

is significantly greater than tidal drag in model simulations of middle atmospheric north

polar warmings during planetary dust events [*Wilson*, 1997; *Forbes and Miyahara*, 2006] but is of comparable magnitude to estimates (-1000 ms^{-1}sol^{-1}) by *Barnes* [1990] of the gravity wave drag necessary to produce up to 50 K departures from radiative equilibrium.

Nevertheless, we would like to emphasize that our quantitative estimates of wave drag are tenuous, since: (1) convective instability is only one process by which tides and gravity waves dissipate; (2) the vertical resolution of MCS may underresolve convective instabilities; (3) and the instability analysis presented above provides very limited information about the characteristics of the waves that produce the observed instabilities and the fullness of their distribution with wavelength, phase speed, and intermittency factor. Thus, any dynamical interpretation that connects (or disconnects) the observed instabilities with the occurrence and vigor of polar warmings is entirely tentative, and thus considerable additional observational and modeling work will be required to demonstrate it.

With these caveats in mind, the interannual variability in the occurrence of convective instabilities in the northern extratropics during northern fall creates a natural sensitivity experiment, in which the potential dynamical influence of the wave drag associated with the observed convective instabilities can be investigated. Figures 3.16a-d show variability in the nightside zonal average temperature structure in four different latitudinal bins, all in the northern hemisphere but ranging from near the pole to the edge of the northern tropics. Temperatures closer to the tropics at $\sim$1—10^{-2} Pa are considerably cooler in northern fall of MY 28 (Figures 3.16c-d) than in northern fall of MY 29. Dayside temperatures at $\sim$1—10^{-2} Pa appear cooler in northern fall of MY 28 as well, but
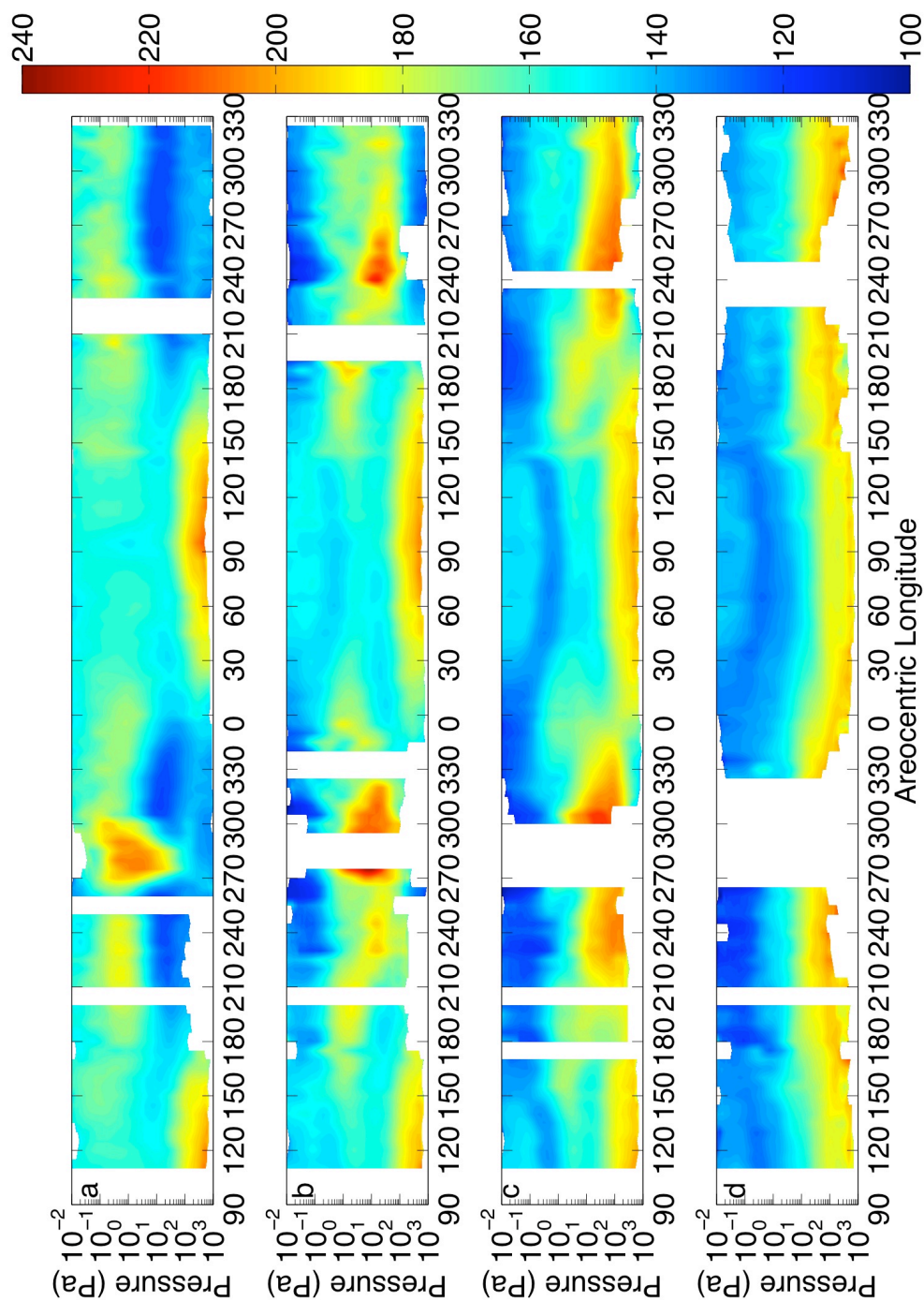
Figure 3.16. Nightside zonal average temperature (K) vs. p and L_s (includes retrievals from limb staring data) for the latitudinal bins: (a) 75°—80° N. (b) 60°—65° N. (c) 45°—50° N. (d) 25°—30° N.

the effects of the tide displace the region of coldest temperatures to lower pressures beyond MCS's vertical range (already limited in limb staring mode). To determine the potential interannual variability in tropical middle atmospheric temperatures more rigorously, we account for the estimated errors in the retrievals.

The random error in an average of independent measurements (applicable since the error at a pressure level is characteristic of an individual retrieval) is found by:

$$\sigma_{avg} = \frac{\sqrt{\sum\limits_{i} \sigma_i^2}}{n} \tag{3.8}$$

where in this case, σ_I is the temperature error in the retrieval and n is the number of retrievals in the average. Recall that this formula is applied twice to determine the error in the zonal average: once to determine the error in each longitudinal bin average and once to determine the error in the zonal average itself. In addition, recall that the error in a difference of independent variables is given by the square root of the sum of the square of their individual errors.

Figures 3.17a-c show the difference (and error estimates) between nightside 0.1 Pa temperatures in MY 28 and 29 in two latitudinal bands near the northern tropic and one latitudinal band just south of the equator. The interannual variability in 0.1 Pa temperatures is fairly similar in all three latitudinal bands. Temperatures during MY 28 and MY 29 are relatively similar until around $L_s=180°$, when MY 28 temperatures become 10—25 K cooler than in MY 29. This drop is not coincident with the change in MCS observing mode between limb scanning and limb staring but occurs before it (Figure 3.17c) or ~10 degrees of L_s after it (Figures 3.17a-b). Temperatures are steadily
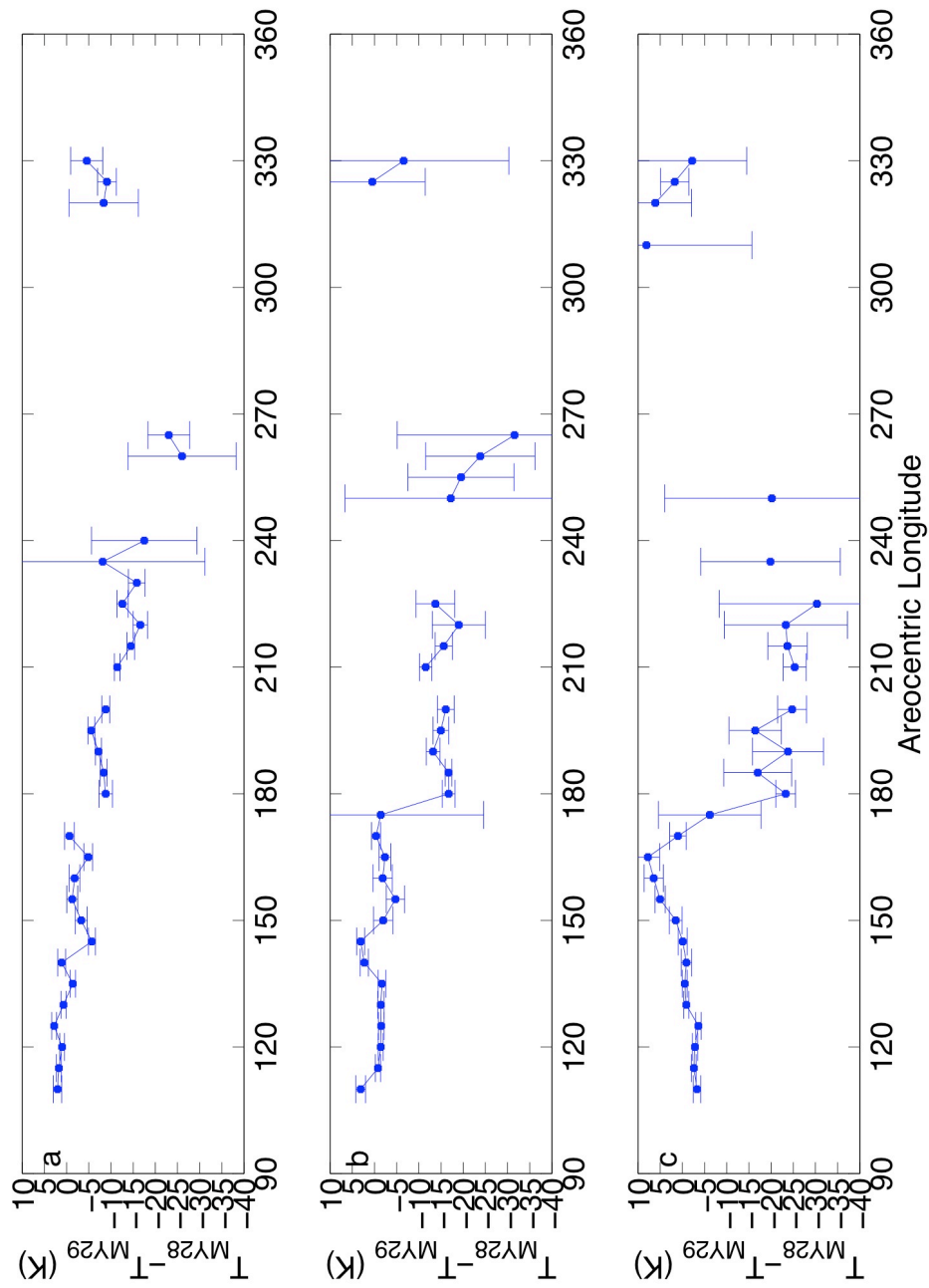
Figure 3.17. Nightside zonal average temperature difference (K) between MY 28 and 29 (K) at 0.1 Pa. The error bars show the 2σ estimate of the error in the temperature difference. (a) 35°—40° N; (b) 25°—30° N; (c) 5°—10° S.

cooler up to $L_S=265°$. When interannual comparison is again possible in late southern summer, 0.1 Pa temperatures are similar in both years. Therefore, tropical temperatures at 10^{-1} Pa at ~3:00 LST were ~25 K cooler during northern fall of MY 28 than during northern fall of MY 29.

These cooler temperatures could be connected to the inferred wave drag in the northern extratropics, which would slow the winter westerly jet and force strong upwelling and adiabatic cooling equatorward of the drag and downwelling/ adiabatic warming poleward. *Forbes and Miyahara* [2006] model an analogous circulation driven by the dissipation of the semi-diurnal tide. The temperature of the feature we attribute to the adiabatic warming (the high latitude polar middle atmospheric temperature maximum) (Figure 3.16a) is similar in both years (before the onset of the planetary dust event), which initially appears inconsistent with this hypothesis. However, the fundamental requirement on a meridional circulation driven by wave drag is that it maintain thermal wind balance consistent with the dragged jet. The thermal wind shear is proportional to the meridional temperature gradient (see Eq. 3.3), i.e., the pole to tropical temperature gradient, which is higher at $1—10^{-2}$ Pa during northern fall of MY 28 than in northern fall of MY 29.

Interannual variability in tropical temperatures at $1—10^{-2}$ Pa during northern fall and winter could have consequences for dust storm activity, in particular the development of the 2007 global dust storm in MY 28. *Rafkin* [2009] has attempted to integrate the proposed hurricane analogy for martian dust storms with thermodynamic models of terrestrial hurricanes. *Rafkin*'s [2009] numerical simulations of small dust storms show that their intensity is dependent on the difference between the inflow temperature of

dusty air at the surface and the outflow temperature of the storm's circulation, as would be expected from a simple Carnot heat engine model. In effect, a steeper lapse rate at the top of the circulation results in a stronger dust storm. The dust storms simulated by *Rafkin* [2009] are relatively small and shallow compared with planetary-scale dust storms on Mars, but the basic heat engine framework may be relevant to these larger circulations, which may penetrate into the middle atmosphere [*Jaquin et al*., 1986; *Newman et al.*, 2002]. Colder temperatures lower in the tropical atmosphere could permit more efficient dust storms if regional dust storm activity that initially develops in the southern mid-latitudes breaks into the tropical middle atmosphere. Thus, strong extratropical wave breaking could prime Mars's atmosphere for planetary-scale dust activity.

3.4.3 Possible Causes for Interannual Variability in Northern Extratropical Instability

Because of its potential significance for global dust storm amplification, it is important to understand why middle atmospheric convective instability in the northern extratropics is so variable between two observed years. Interannual variability may arise most immediately from the lower mean stability in the northern extratropics at a level of ~1—0.1 Pa during MY 28 (Figures 3.10a-b), which could allow even a uniform gravity wave flux to saturate more easily. These differences are not limited to the northern extratropics. There is an unstable region at ~1 Pa in the southern tropics (Figures 3.10a and 3.10e) during northern fall of MY 28 that is not apparent in MY 29 (Figure 3.10b). The zonal average stability structure is related to both the mean meridional circulation

and the thermal tides, both of which can be affected by gravity wave drag on the zonal wind field, raising the possibility of feedback.

In addition, the gravity wave flux itself is probably variable. The lowest zonal average $\Gamma(p < 50$ Pa), when longitudinal sampling is complete or nearly so, is rarely less than 2 K km^{-1} in both the northern and southern extratropics. In these cases, zonal average CAPE$_{MA}$ can vary by more than an order of magnitude for the same minimum zonal average $\Gamma(p < 50$ Pa) and is generally highest in the northern extratropics during MY 28.

Interannual variability in gravity wave flux and changes in gravity flux before or after a global dust storm could be related to interannual variability in (1) baroclinic wave activity [*Barnes*, 1980, 1981]; or (2) moist carbon dioxide convection in polar night [*Cornwall and Titus*, 2009]. However, a connection between these phenomena and gravity wave generation has not been established for Mars, so a definite explanation for the interannual variability in middle atmospheric convective instability in the northern extratropics will require considerable additional research.

3.5. Summary

I have detected widespread convective instability or near-instability within Mars's middle atmosphere, which I propose is the result of gravity wave saturation modulated by the thermal tides. I am able to characterize much of this instability's spatial and temporal variability. The most notable aspect of this variability is the contrast between the northern and southern extratropics. During both years of observation, middle atmospheric convective instability was moderately frequent in the southern extratropics during

southern fall and winter. In the northern extratropics, middle atmospheric convective instability was at the highest levels observed anywhere on the planet between the beginning of the fall and the onset of the 2007 global dust storm, at which point it fell to relatively low levels and continued at low levels even in northern winter of the next year. At the minimum, this contrast suggests that gravity wave sources and propagation conditions can differ greatly between northern fall and winter and southern fall and winter on Mars and in the same hemisphere during different years.

While the estimates of the wave drag on the atmospheric circulation in this study are highly tentative, the interannual variability in convective instability in the northern extratropics may provide a potential insight into the effect of extratropical wave drag on the circulation. During MY 28, strong wave drag may have strengthened middle atmospheric upwelling at the equator and produced an observed cooling of northern mid-latitude and tropical middle atmospheric temperatures, which could have favored development of a global dust storm in MY 28.

The existence of a possible gravity wave saturation signal such as convective instability in MCS retrieved temperature profiles and its potential dynamical importance should motivate further efforts to observe tidal and gravity wave dissipation in the martian atmosphere. One future area of investigation could be analysis of the brightness temperature variances in limb-sounding and airglow data, which is a standard technique for investigating gravity waves in the Earth's atmosphere and may allow easier distinction of the relative role of gravity waves and the tides, surer connection with gravity wave sources, and easier quantification of the profile of dissipation than possible

in this study [*Wu and Waters*, 1996; *Fritts and Alexander*, 2003]. MCS calibrated

radiance data could be useful in this regard.

Bibliography

Barnes J. R. (1980), Time spectral analysis of midlatitude disturbances in the Martian atmosphere, *J. Atmos. Sci.*, *37*, 2002–2015.

Barnes J. R. (1981), Midlatitude disturbances in the Martian atmosphere: A second Mars year. *J. Atmos. Sci.*, *38*, 225–234.

Barnes, J.R. (1990), Possible effects of breaking gravity waves on the circulation of the middle atmosphere of Mars, *J. Geophys. Res., 95* (B2), 1401-1421.

Bücker, D., R. Span, and W. Wagner (2003), Thermodynamic Property Models for Moist Air and Combustion Gases, *J. Eng. Gas Turbines Power*, *125*(1), 374-384.

Cantor, B., M. Malin, and K.S. Edgett (2002), Multiyear Mars Orbiter Camera (MOC) observations of repeated Martian weather phenomena during the northern summer season, *J. Geophys. Res.*, *107*(E3), 5014, doi:10.1029/2001JE001588.

Clancy, R.T., B.J. Sandor, M.J. Wolff, P.R. Christensen, M.D. Smith, J.C. Pearl, B.J. Conrath, and R.J. Wilson (2000), An intercomparison of ground-based millimeter, MGS TES, and Viking atmospheric temperature measurements: Seasonal and interannual variability of temperatures and dust loading in the global Mars atmosphere, *J. Geophys. Res., 105*, 9553–9571

Clancy, R.T., M.J. Wolff, B.A. Whitney, B.A. Cantor, and M.D. Smith (2007), Mars equatorial mesospheric clouds: Global occurrence and physical properties from Mars

Global Surveyor Thermal Emission Spectrometer and Mars Orbiter Camera limb observations, *J. Geophys. Res*., *112*, E04004, doi:10.1029/2006JE002805.

Collins, M., S.R. Lewis, and P.L. Read (1997), Gravity wave drag in a global circulation model of the Martian atmosphere: Parametrisation and validation, *Adv. Space. Res.*, *44*, 1395–1409.

Collins, R.L. and R.W. Smith (2004), Evidence of damping and overturning of gravity waves in the arctic mesosphere: Na lidar and OH temperature observations, *J. Atmos. Solar-Terrest. Phys., 66* (10), 867-879.

Cornwall, C. and T.N. Titus (2009), Spatial and temporal distributions of Martian north polar cold spots before, during, and after the global dust storm of 2001, *J. Geophys. Res.*, *114*, E02003, doi:10.1029/2008JE003243.

Creasey, J.E., J.M. Forbes, and D.P. Hinson (2006), Global and seasonal distribution of gravity wave activity in Mars' lower atmosphere derived from MGS radio occultation data, *Geophys. Res. Lett.*, *33*, L01803, doi:10.1029/2005GL024037.

Deming, D., M.J. Mumma, F. Espenak, T. Kostiuk, and D. Zipoy (1986), Polar warming in the atmosphere of Mars, *Icarus*, *66*, 366-379.

Forbes, J.M., and S. Miyahara (2006), Solar Semidiurnal Tide in the Dusty Mars Atmosphere, *J. Atmos. Sci.*, *63* (7), 1798-1817.

Forget, F., F. Hourdin, R. Fournier, C. Hourdin, O. Talagrand, M. Collins, S.R. Lewis, P.L. Read, and J.-P. Huot (1999), Improved general circulation models of the Martian atmosphere from the surface to above 80 km, *J. Geophys. Res.*, *104*, 24,155–24,176.

Fritts, D.C. and M.J. Alexander (2003), Gravity wave dynamics and effects in the middle atmosphere, *Rev. Geophys.*, *41* (1), doi:10.1029/2001RG000106.

Fritts, D.C., L. Wang, and R.H. Tolson (2006), Mean and gravity wave structures and variability in the Mars upper atmosphere inferred from Mars Global Surveyor and Mars Odyssey aerobraking densities, *J. Geophys. Res.*, *111*, A12304, doi:10.1029/2006JA011897.

Hartogh, P., A.S. Medvedev, and C. Jarchow (2007), Middle atmospheric polar warmings on Mars: Simulations and study on the validation with submillimeter observations, *Adv. Space. Res*, *55*, 1103-1112.

Hinson, D.P., M. Pätzold, S. Tellmann, B. Hausler, and G.L. Tyler (2008), The depth of the convective boundary layer on Mars, *Icarus*, *198,* 57-66.

Hodges, R.R., Jr. (1967), Generation of turbulence in the upper atmosphere by internal gravity waves, *J. Geophys. Res.*, *72*, 3455-3458.

Holton, J.R. (2004), *An Introduction to Dynamic Meteorology*, 4th Edition, Elsevier, Amsterdam.

Inada, A., M.I. Richardson, T.H. McConnochie, M.J. Strausberg, H. Wang, and J.F. Bell (2007), High-resolution atmospheric observations by the Mars Odyssey Thermal Emission Imaging System, *Icarus*, *192* (2), 378-395.

Jaquin, R.F. III (1989) The middle Martian atmosphere, Ph.D. Thesis, 122 pp., Cornell University, Ithaca, NY, September.

Jaquin, R.F. III, P. Gierasch, and R. Kahn (1986), The vertical structure of limb hazes in the Martian atmosphere, *Icarus*, *72*, 528-534.

Joshi, M. M., B.N. Lawrence, and S.R. Lewis (1995), Gravity wave drag in three-dimensional atmospheric models of Mars, *J. Geophys. Res.*, *100*, 21,235–21,245.

Kleinböhl, A., J.T. Schofield, D.M. Kass, W.A. Abdou, C.R. Backus, B. Sen, J.H. Shirley, W.G. Lawson, M.I. Richardson, F.W. Taylor, N.A. Teanby, and D.J. McCleese (2009), Mars Climate Sounder limb profile retrieval of atmospheric temperature, pressure, dust and water ice opacity, *J. Geophys. Res., 114*, E10006, doi:10.1029/2009JE003358.

Knudsen, W.C. and G.W. Sharp (1965), Evidence for temperature stratification in the E region, *J. Geophys. Res.*, *70*, 143-160.

Lee, C., W.G. Lawson, M.I. Richardson, N.G. Heavens, A. Kleinböhl, D. Banfield, D.J. McCleese, R. Zurek, D. Kass, J.T. Schofield, C.B. Leovy, F.W. Taylor, A.D. Toigo, (2009), Thermal tides in the Martian middle atmosphere as seen by the Mars Climate Sounder, *J. Geophys. Res.*, *114*, E03005, doi:10.1029/2008JE003285.

Lindzen, R.S. (1981), Turbulence and Stress Owing to Gravity Wave and Tidal Breakdown, *J. Geophys. Res.*, *86*(C10), 9707–9714.

Liu, A. Z., R.G. Roble, J.H. Hecht, M.F. Larsen, and C.S. Gardner (2004), Unstable layers in the mesopause region observed with Na lidar during the Turbulent Oxygen Mixing Experiment (TOMEX) campaign*, J. Geophys. Res., 109*, D02S02, doi:10.1029/2002JD003056.

Liu, J., M.I. Richardson, and R.J. Wilson (2003), An assessment of the global, seasonal, and interannual spacecraft record of Martian climate in the thermal infrared, *J. Geophys. Res., 108*(E8), 5089, doi:10.1029/2002JE001921.

McCleese, D. J., J.T. Schofield, F.W. Taylor, S.B. Calcutt, M.C. Foote, D.M. Kass, C.B. Leovy, D.A. Paige, P.L. Read, and R.W. Zurek (2007), Mars Climate Sounder: An investigation of thermal and water vapor structure, dust and condensate distributions in the atmosphere, and energy balance of the polar regions, *J. Geophys. Res., 112*, E05S06, doi:10.1029/2006JE002790.

McCleese, D.J., J.T. Schofield, F.W. Taylor, W.A. Abdou, O. Aharonson, D. Banfield, S.B. Calcutt, N.G. Heavens, P.G.J. Irwin, D.M. Kass, A. Kleinböhl, W.G. Lawson, C.B. Leovy, S.R. Lewis, D.A. Paige, P.L. Read, M.I. Richardson, N. Teanby, and R.W. Zurek (2008), *Nature Geosci., 1*, 745-749, doi:10.1038/ngeo332.

Montmessin, F., B. Gondet, J.-P. Bibring, Y. Langevin, P. Drossart, F. Forget, and T. Fouchet (2007), Hyperspectral imaging of convective CO_2 ice clouds in the equatorial mesosphere of Mars, *J. Geophys. Res.*, *112*, E11S90, doi:10.1029/2007JE002944.

Newman, C.E., S.R. Lewis, P.L. Read, and F. Forget (2002), Modeling the Martian dust cycle: 2. Multi-annual radiatively active dust transport simulations, *J. Geophys. Res.*, *107* (E12), 5124. doi:10.1029/2002JE001920.

Rafkin, S.C.R. (2009), A Positive Radiative-Dynamic Feedback Mechanism for the Maintenance and Growth of Martian Dust Storms. *J. Geophys. Res.*, *114*, E01009, doi:10.1029/2008JE003217.

Richardson, M.I. (1998), Comparison of Microwave and Infrared Measurements of Martian Atmospheric Temperatures: Implications for Short-Term Climate Variability, *J. Geophys. Res.*, *103*(E3), 5911-5918.

Sica, R. J., and M.D. Thorsley (1996), Measurements of superadiabatic lapse rates in the middle atmosphere, *Geophys. Res. Lett.*, *23*(20), 2797–2800.

Span, R. and W. Wagner (1996), A New Equation of State for Carbon Dioxide Covering the Fluid Region from the Triple-Point Temperature to 1100 K at Pressures up to 800 MPa, *J. Phys. Chem. Ref. Data*, *25*, 1509, doi:10.1063/1.555991.

Theodoré, B., E. Lellouch, E. Chassefiére, and A. Hauchecorne (1993), Solstitial Temperature Inversions in the Martian Middle Atmosphere, *Icarus*, *105*(2), 512-528.

Wang, L., D.C. Fritts, and R.H. Tolson (2006), Nonmigrating tides inferred from the Mars Odyssey and Mars Global Surveyor aerobraking data, *Geophys. Res. Lett.*, *33*, L23201, doi:10.1029/2006GL027753.

Whiteway, J.A., and A.I. Carswell (1994), Rayleigh Lidar Observations of Thermal Structure and Gravity Wave Activity in the High Arctic during a Stratospheric Warming. *J. Atmos. Sci.*, 51, 3122–3136.

Williams, B. P., M.A. White, D.A. Krueger, and C.Y. She (2002), Observation of a large amplitude wave and inversion layer leading to convective instability in the mesopause region over Fort Collins, CO (41°N, 105°W), *Geophys. Res. Lett.*, *29*(17), 1850, doi:10.1029/2001GL014514.

Williams, B.P., D.C. Fritts, C.Y. She, and R.A. Goldberg (2006), Gravity wave propagation through a large semidiurnal tide and instabilities in the mesosphere and lower thermosphere during the winter 2003 MaCWAVE rocket campaign, *Ann. Geophys.*, *24*, 1199-1208.

Wilson, R.J. (1997), A general circulation model of the Martian polar warming, *Geophys. Res. Lett.*, *24*, 123–126.

Wilson, R.J. and M.I. Richardson (2000), The Martian Atmosphere during the Viking Mission, 1, Infrared Measurements of Atmospheric Temperatures Revisited, *Icarus*, *145*, 555-579.

Wu, D.L. and J.W. Waters (1996), Gravity-Wave-Scale Temperature Fluctuations Seen

by the UARS MLS, *Geophys. Res. Lett.*, *23*(23), 3289–3292

Zurek, R.W. (1976), Diurnal tide in the Martian atmosphere, *J. Atmos. Sci.*, *33*, 321-337.

Zurek, R.W. and S.E. Smrekar (2007), An Overview of the Mars Reconnaissance Orbiter (MRO) Science Mission, *J. Geophys. Res. Planets*, 112, E5, doi: 10.1029/2006JE002701.